Review article

Metallic nanoparticles and hybrids of metallic nanoparticles/ graphene nanomaterials for enhanced photon harvesting and charge transport in polymer and dye sensitized solar cells

Tabitha A. Amollo

Department of Physics, Egerton University, Egerton, Kenya

A R T I C L E   I N F O

A B S T R A C T

Solar energy is a sustainable option in the provision of affordable and clean energy. Conversion of solar energy to electricity requires the development of materials and technologies that are not only efficient but also cost-effective. Polymer solar cells (PSCs) and dye sensitized solar cells (DSSCs) are some of the cost-effective technologies for solar energy conversion. However, PSCs suffer from poor optical absorption and charge carrier mobility, while the major drawback to high efficiencies in DSSCs is charge carrier recombination. This article examines the potency of plasmonic metallic nanoparticles (MNPs) and hybrids of MNPs/graphene nanomaterials (GNMs) in mitigating these challenges. MNPs and MNPs/GNMs incorporated in these devices enhance light harvesting to extended wavelengths and improve charge transport. MNPs in the photoanode of DSSCs serve as cosensitizers to offer complementary optical absorption, while MNPs/GNMs as counter electrode yield high catalytic activity comparable to Pt. Simultaneous application of MNPs and/or MNPs/GNMs in PSCs' interfacial and active layers yield enhanced broadband optical absorption and effective charge transport. The mechanisms by which these nanomaterials enhance light harvesting in these devices are discussed in detail. The material characteristics that influence the performance of MNPs and MNPs/GNMs modified devices, such as MNPs size, shape, and morphology, are highlighted. Hence, this article presents perspectives and strategies on successful utilization of plasmonic MNPs and hybrids of MNPs/GNMs to mitigate the challenges of poor optical absorption and charge transport of PSCs and DSSCs for high efficiencies.

1. Introduction

Nanoscale science and technology, known as nanotechnology, has technologically revolutionized the world. This science entails the preparation, characterization, and manipulation of structures of particles/materials in the nanometre scale, typically in the range of 1–100 nm. Nanoscale research field is evolving fast, fuelled by the desire for functional materials with novel/improved properties. These properties include electronic transport, optical response, mechanical strength, elasticity, and thermal conductivity. Such functional nanomaterials find application in various fields including biomedicine, electronics, optoelectronics, energy conversion and storage, and magnetic applications. For example, in microelectronics, the use of nanomaterials has led to the evolution of miniaturization trends i.e., the fabrication of integrated circuits and storage media in the nanoscale has resulted in 'smaller' computers with high computational power. These functional materials include carbon-based nanomaterials, nanoparticles, nanocomposites, and

quantum dots.

Nanotechnology has revolutionized the development of solar cells from the second to the current fourth generation. This is because an improvement in the performance of solar cells requires materials development and device engineering. The second-generation solar cells are constituted by thin-film technology that utilizes inorganic compounds like amorphous silicon (a-Si:H), gallium arsenide (GaAs) and cadmium telluride (CdTe). Polymer solar cells (PSCs) and dye sensitized solar cells (DSSCs), together with quantum dot and multijunction solar cells, form the third-generation solar cells. The fourth generation comprises perovskite solar cells (PVSCs) and a class of PSCs with a polymer: nanoparticle blend in the photoactive layer. The solution processable PSCs, DSSCs, and PVSCs are advantageous in terms of cost-effectiveness i.e., they can be produced from readily available and/or cheap materials using simple techniques, mechanical flexibility, lightweight, large area applications, and environmental friendliness. These have advanced the prospects for the provision of clean and affordable energy needed to meet the requirements of energy security and environmental safety, for a technologically fast-paced world. The third and fourth-generation solar cells are under intensive research to achieve high solar energy conversion efficiencies (PCEs). To this end, developing functional energy materials and device engineering is imperative. Graphene nanomaterials and metallic nanoparticles are among the materials under extensive research, for application in these solar cells.

Graphene, a monolayer of carbon atoms packed in a honeycomb hexagonal structure, is characterized by unique properties, including high specific surface area, carrier mobility, optical transparency, thermal conductivity and material strength and flexibility [1]. These properties suit it for application in energy conversion and storage, sensors for biomedical applications, photodetectors, and nanoelectronics [1]. Pristine graphene, though characterized with ballistic charge carriers transport resulting in excellent electronic transport i.e. charge carrier mobility as high as 200,000 $cm^2V^{-1}s^{-1}$, [2] and electrical resistivity of $10^{-6}\Omega cm$, [3] has no energy band gap thus, is limited in optoelectronics and nanoelectronics applications. Besides being hydrophobic, pristine graphene is neither compatible with cost-effective solution phase synthesis nor solution-based device processing. For these reasons, functionalized forms of graphene come in handy for practical applications. Functionalized graphene includes graphene oxide (GO) and nitrogen-doped graphene (NGr). GO extends the functionality of graphene as its oxygen-functionalized groups including the epoxy, carboxylic and hydroxyl, provide nucleation sites for further functionalization [4]. This way graphene can be combined with other materials like metallic nanoparticles (MNPs) and polymers for synergy of the unique properties for specific applications. Additionally, GO being hydrophilic is compatible with solution-based device processing.

Nanoparticles are characterized by unique morphological properties, particle size distribution, and size quantization effects such as quantum confinement and tunnelling of charge carriers. Further, these class of materials have high surface reactivity which originates from their inherent high specific surface area to volume ratio (aspect ratio) [5]. MNPs are formed from noble metals like gold, copper, silver, iron, and platinum or their compounds like sulphides, oxides, fluorides, and phosphates. These find application in biomedicine, photocatalysis, sensors, optics [6] and solar cells [7]. Furthermore, the MNPs in combination with other materials like carbon-based materials or polymers can be synthesized into nanocomposites with tailored properties for specific applications. Hybrids of MNPs and graphene nanomaterials (GNMs) like GO, graphene quantum dots (GQDs) and reduced graphene oxide (rGO), because of their synergistic properties, find application in sensors [8,9], electronics [10], biomedicine [10], energy conversion [11], catalysis [10], and in removal of environmental pollutants [12], depending on the MNPs composition. For example, hybrids of GO and plasmonics have unique properties including high specific surface area, chemical and electrochemical inertness which suit them for use in biosensors and surface enhanced Raman spectroscopy (SERS) for early stage medical conditions diagnosis [13]. This review focuses on applying MNPs and hybrids of MNPs/(GNMs) in PSCs and DSSCs. MNPs exhibit plasmonic effects, one of their main desirable properties for application in solar energy conversion devices.

2. Localized surface plasmon resonance in metallic nanoparticles

Surface plasmon resonance (SPR) is a coherent oscillation of metal conduction electrons produced upon excitation by an incident electromagnetic radiation at a metal-dielectric interface. These oscillations yield a short-lived electric field within the dielectric extending from the metal surface to a hundred nanometres length scale [14]. There are two types of SPRs, *viz.* Surface plasmon polaritons (SPPs) which are propagating, and localized SPRs which are non-propagating. The SPPs propagate tens to hundreds of micrometres along a MNPs surface with an exponentially decaying electric field. Excitation of SPPs can be achieved by utilizing prism couplers or gratings [15]. Local surface plasmons are produced when the wavelength of the incident light is greater than the metal particle size [16]. This give rise to a non-propagating plasmon that oscillates within the MNPs vicinity with a frequency of localized surface plasmon resonance (LSPR) [17]. Equation (1) gives the energy of this plasmon according to the free electron model [18].

$$E_p = \hbar \sqrt{\frac{ne^2}{m\varepsilon_o}} = \hbar\omega_p \tag{1}$$

Where n is the density of electrons, e is the electron charge, m is the electron mass, ε_o is the permittivity of free space, $\hbar$ is Planck constant and ω_p the bulk plasmon frequency.

Typically, MNPs exhibit LSPRs when the frequency of the incident photon is resonant with the cumulative oscillation of the conduction electrons within the nanoparticle volume. Silver and gold nanoparticles manifest strong LSPR within the visible region of the electromagnetic spectrum [19]. The magnitude and spectral position of LSPR is dependent on the local dielectric medium and the nanoparticle's size, shape, aspect ratio and composition [6].

Dipole LSPR, the simplest LSPR occurs in the limit where the particle's diameter is smaller than the incident photon's wavelength.

The conduction electrons in the MNPs will oscillate in phase upon the plane wave excitation. This produces a build-up of polarization charges on the particle's surface, which causes a resonance to appear at a particular frequency referred to as particle dipole plasmon frequency [20,21] This frequency is determined by the density of electrons, the size and shape of charge distribution and the effective mass of the electron [22]. Consequently, a homogenous resonant electric field builds up within the nanoparticle, and a dipolar field builds up outside of it. This yields strong surface plasmon absorption bands, intense light scattering and an enhanced electric field near the particle surface [19,21]. Thus, MNPs can be used to guide and focus light, and alter the absorption or emission of light to the nanometre scale in a nearby optically active medium within its vicinity. As such, MNPs come in handy in improving photon harvesting in solar cells. The plasmonic effects *viz.* The wavelength at which maximum absorption occurs, and the peak height and bandwidth are dependent on the NPs size, geometry, composition, and dielectric environment. For example, for larger MNPs higher order LSPRs such as quadrupole whereby the motion of half of the electron cloud is parallel and the other half antiparallel, are excited thus modifying the spectroscopic responses [22]. MNPs find application in solution-processable thin film solar cells (TFSCs), including PSCs, PVSCs and DSSCs.

Table 1
Metallic nanoparticles synthesis methods.

Method	Examples	Advantages	Disadvantages	References
Bottom-up methods				
Solid-state synthesis methods	Chemical vapour deposition	Allows for control of nanoparticle structure. Produces durable thin films. Scalable	Is toxic. Is complex	[25]
	Physical vapour deposition	Simple	Costly Not suitable for large-scale production	[26] [27]
Solution-phase synthesis	Sol-gel method	Very simple Allows for control of nanoparticle size and morphology		[28] [29]
	Solvothermal method	Produces high-quality crystallized nanoparticles of narrow size distribution		[30]
	Chemical reduction method	Very simple Shortcomings associated with reducing agents, e.g., toxicity, impurities, and high costs		[31] [32]
	Hydrothermal method	Allows for control of nanoparticles size and shape. Produces highly crystalline nanoparticles	Difficulty in controlling the process. Difficult to reproduce	[33]
Gas phase synthesis methods	Laser pyrolysis	Produces nanoparticles of uniform size distribution Allows for control of nanoparticles size. Suitable for large scale production		[34] [35]
	Spray pyrolysis	Simple Cheap Allows for control of nanoparticles size		[36] [37]
Top-down methods				
Mechanical methods	Ball milling	Capable of large-scale production Produces high purity nanoparticles	Utilizes high energy. Time-consuming Possible contamination of samples by the steel balls	[38] [39]
	Mechanochemical method	Simple and efficient	Possible contamination of samples Time-consuming	[40] [41]
Ion sputtering		Associated with less impurities in comparison to chemical methods. Versatile for preparation of ionic nanoparticles of various sizes Allows for control of nanoparticles size, composition, and ion charge	The morphology, composition and optical properties of produced nanoparticles can be affected by the nature of the sputtering gas	[42] [43]
Laser ablation		Simple Allows for control of nanoparticles properties by selecting appropriate laser parameters. Capable of large-scale production	Not efficient as large number of nanoparticles block the laser path and absorb laser energy	[44] [45] [46]
Scanning beam lithography		**Allows for the control of size and structure of the nanoparticles**		[47] [48]

3. Preparation methods for metallic nanoparticles and hybrids of metallic nanoparticles/graphene materials

3.1. Preparation techniques for metallic nanoparticles

Physical and chemical methods are commonly employed for the preparation of MNPs. These are broadly classified into two categories: top town and bottom-up methods as listed in Table 1. The starting material is the major difference between these two synthesis approaches. The starting material for the top-down methods is in bulk form which is then reduced to nanoparticles by physical, mechanical or chemical process while atoms/molecules form the starting material for bottom-up approaches [23]. The preparation technique used directly influences the nanoparticle's size, shape, morphology, and physicochemical properties through the different kinetic and adsorption processes involved [24]. In turn, the size, morphology and composition influence nanoparticles' optoelectronic and catalytic properties [6]. Thus, choosing an appropriate methodology is important in producing MNPs for specific applications. For example, the Au nanoparticles shown in Fig. 1 were prepared by a seed-based method. The nanoparticles sensitivity for plasmonic sensing applications, was found to be mainly dependent on their aspect ratio.

3.2. Preparation techniques for hybrids of metallic nanoparticles/graphene nanomaterials

The synthesis methods for the hybrids of MNPs and GNMs can generally be classified into two categories *viz. ex situ* and *in situ*. Preformed MNPs are utilized in the *ex situ* methods whereas GNMs forms the substrate on which MNPs are grown in the *in situ* methods. The *ex situ* approach is advantageous in terms of uniformity in the preformed nanoparticles size, shape and morphology, consistency in materials properties and elimination of incompatibility that may arise during material growth [49]. Mostly, the *in situ* methods produce polydisperse nanoparticles with varied shapes [50]. MNPs/GNMs hybrids can be synthesized successfully in liquid-phase using preformed MNPs and graphene derivatives as the substrates. The liquid-phase synthesis route is simple, does not require expensive equipment and is capable of large-scale production. The major components in this synthesis method are the preformed metallic nanoparticles, solvent system, ligand stabilizers and the graphene substrates. The graphene derivatives GO and rGO form an excellent platform for loading MNPs because of their high specific surface area and rich oxygen functional groups as highlighted in section 1. The methods used for immobilization of MNPs on GO sheets include chemical reduction method, microwave or light irradiation method and thermal assisted method. Of these, chemical reduction is the commonly used method because it is cost-effective and simple. This method involves the reduction of metal ion salts in solution form to MNPs on GO sheets using reducing agents such as hydrazine, ascorbic acid, and sodium borohydride. Typically, the noble metal salt solution is first thoroughly mixed with the GO dispersion. In this process, the noble metals ions would adsorb on the GO sheets. Finally, the reducing agents reduces the noble metals ions adsorbed onto the GO nanosheets to MNPs [51]. Immobilization of MNPs on GO sheets by the light irradiation method is eco-friendly and allows for the control of MNPs size and distribution by varying the intensity and time of irradiation as shown in Fig. 2 (A-J) [52]. Similarly, microwave irradiation method allows for control of the MNPs size and distribution and is environmentally friendly [53]. Nonetheless, the light or microwave irradiation methods are not cost-effective as they utilize equipment that requires energy input. The thermal-assisted method, though simple, requires energy input for heating the precursors at elevated temperatures [54]. Both the thermal assisted and chemical reduction methods do not allow for the control of MNPs size and distribution as they are rapid processes. Moreover, some of the reducing agents like hydrazine used in these processes are harmful to the environmental.
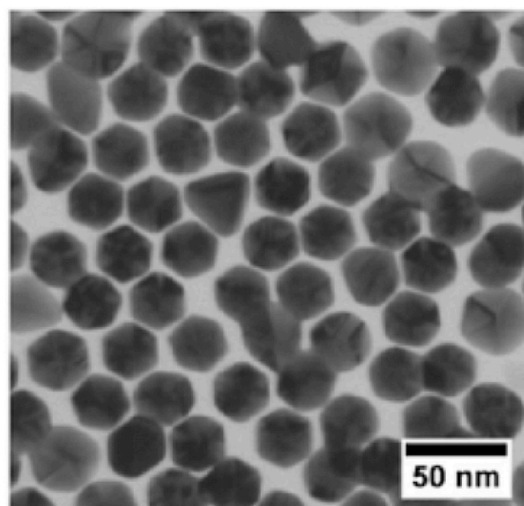

Fig. 1. TEM image of Au nanoparticles. (Reprinted with permission from (Khan et al.) Copyright (2016), American Chemical Society) [6].
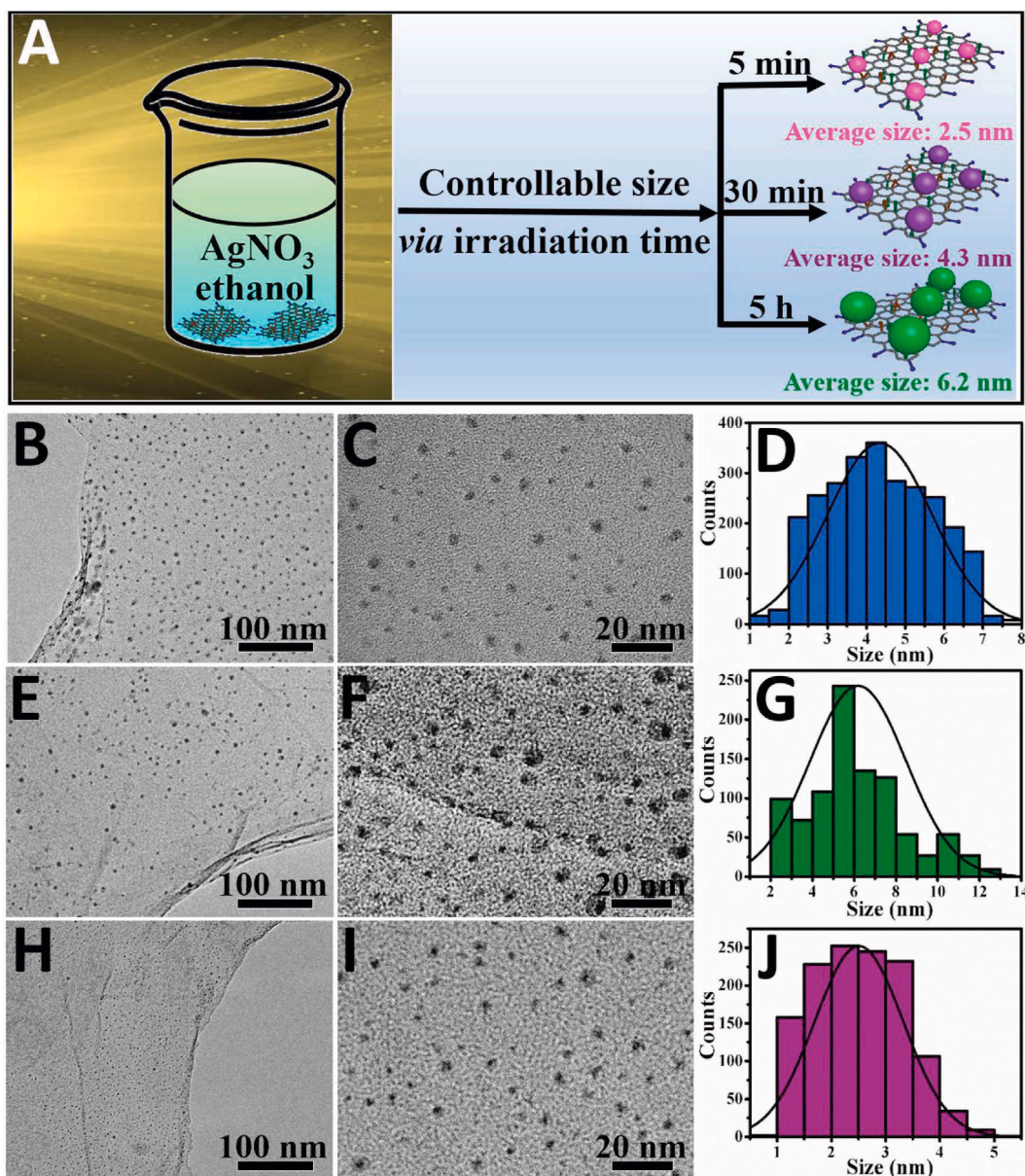
Fig. 2. (A) Schematic diagram of light irradiation synthesis of Ag/GO nanocomposite showing control of MNPs size by varying the irradiation time (B) TEM image (C) HR-TEM image and (D) histogram showing the size distribution of the nanocomposite synthesized by irradiation for 30 min. (E–G) and (H–J) show the corresponding images and size histograms of the nanocomposites synthesized by irradiation for 5 h and 5 min, respectively [52].

4. 4.Application of metallic nanoparticles and hybrids of metallic nanoparticles/graphene nanomaterials in polymer solar cells

PSCs are mostly fabricated in bulk-heterojunction (BHJ) device structure. This structure has five components namely: electrodes (anode and cathode), active layer, hole transport layer (HTL) and electron transport layer (ETL) which can be fabricated in the conventional or inverted device structures as shown in Fig. 3(a) and (b), respectively. The active layer consists of donor and acceptor materials. Upon photoirradiation of the device, excitons are generated in the active layer. These are transported *via* charge percolation pathways to the donor-acceptor interphase where charge separation occurs. The charge carriers i.e. electrons and holes are then transported through the ETL and HTL to the cathode and anode, respectively. The active layer materials should be characterized by high optical absorption and charge carrier mobility. On the other hand, the interfacial layers (ETL and HTL) materials should exhibit good charge transport properties, form an ohmic contact and offer charge selectivity at the active layer-electrodes interfaces. The
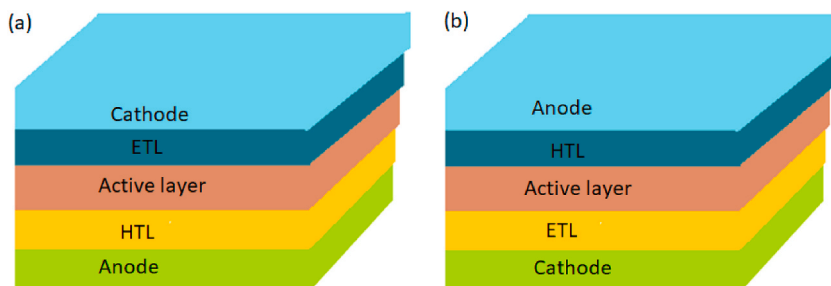
Fig. 3. Schematic diagram of (a) conventional and (b) inverted bulk-heterojunction PSCs.

photovoltaic performance of solar cells is characterized by short-circuit current density, J_{sc}, open-circuit voltage, V_{oc}, fill-factor, FF, and the ultimate power conversion efficiency, PCE. The PSCs discussed herein are of the conventional BHJ structure unless stated otherwise.

4.1. Application of metallic nanoparticles in polymer solar cells

MNPs exhibiting LSPR are suited for use in the interfacial and photoactive layers of PSCs.
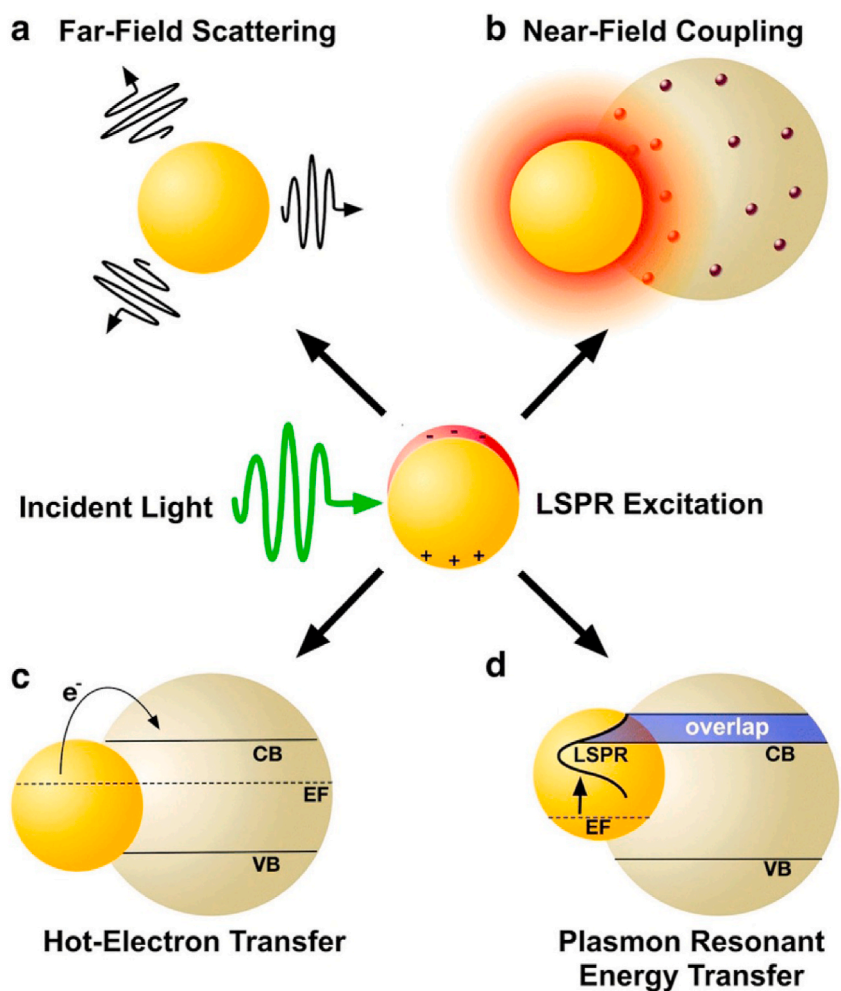

Fig. 4. Mechanisms of plasmon-induced photon harvesting in solar cells [71].

4.1.1. Active layer

In the photoactive medium, MNPs promote light harvesting *via* enhanced light scattering (far-field scattering), near-field effect, plasmon-induced charge separation and creation of strong optical absorption bands. These processes classified as radiative (far-field scattering and near-field effect) and non-radiative (plasmon resonant and hot electron energy transfer) are highlighted in Fig. 4. An enhanced light scattering increases the optical path length thereby allowing for more photon absorption. The scattering (C_{scat}) and absorption (C_{abs}) cross-sections for NPs with wavelengths much less than the incident light wavelength, λ, are given in equations (2) and (3), respectively [20].

$$C_{scat} = \left(\frac{1}{6\pi}\right)\left(\frac{2\pi}{\lambda}\right)^4 |\alpha|^2 \tag{2}$$

$$C_{abs} = \frac{2\pi}{\lambda} Im[\alpha] \tag{3}$$

where $\alpha = 3V\left[\frac{\frac{\varepsilon_p}{\varepsilon_m}-1}{\frac{\varepsilon_p}{\varepsilon_m}+2}\right]$ is the polarizability of the particle, V is the particle volume, ε_p and ε_m.

are the dielectric function of the particle and the surrounding media, respectively. $\varepsilon_p = -2\varepsilon_m$ is the condition necessary for inducing LSPR as the particle polarizability becomes very large [55]. Also, C_{scat} should be greater than C_{abs} for effective light trapping [56]. The scattering efficiency is given by equation (4) [19].

$$Q_{scat} = \frac{C_{scat}}{C_{scat} + C_{abs}} \tag{4}$$

The nanoparticles composition, size, shape, and position in the PSCs affect the light trapping efficiency. For example, Ag produces better path length enhancement than Au [57]. Nanospheres are the most utilized for light scattering though, cylindrical and hemispherical MNPs are more effective in enhancing the optical path length as shown in Fig. 5 [58]. The nanospheres are advantageous in terms of ease in production. Fig. 5 also shows that 100 nm sized NPs are more effective in light scattering than 150 nm sized ones. Baek et al. [59] investigated the influence of Ag NPs size on scattering efficiency by utilizing Ag NPs sized between 13 and 94 nm in the HTL of PSCs. The highest optical absorption of the devices was observed at 67 nm. Beyond this size, the NPs exhibited lower optical absorption due to increased back reflection. For the optical absorption enhancement by NPs scattering, it is important to consider not only the scattering power but also the scattering direction. This is because back scattering does not usually contribute to enhanced optical absorption enhancement, though, it is predominant in larger sized NPS. Thus, the NPS size should be optimized to promote forward scattering. The light scattering effect produced in the active layer requires the MNPs to be placed not directly in the active layer, as this would promote charge carrier recombination. On the other hand, placing the NPs on the rear side of the devices allows for light absorption within a wide range of wavelength. The semiconductor material would absorb the short wavelength light. At the same time, the NPs would promote absorption of the long wavelength light, i.e. the infrared and red light reaching the rear of the solar cells would be scattered and trapped within the device [60]. Also, the position of the MNPs should be such as to allow for a match of the wavelength range to the dipole oscillation [61].

MNPs mixed in the active layer blend or embedded in the active layer promote light trapping by creation of strong electromagnetic field within their vicinity. This way, the optical absorption of the active layer materials is enhanced by the high density of states (DOS) of phonons and by the excitation of charge carriers by the MNPs [62]. The near-field effect is pronounced in small-sized MNPs. The small size and small interspacing distance between the NPs inherently enhance the near-field effect. This effect is compatible and suitable for active layer materials with a short charge carrier diffusion length such as in PSCs. It is also compatible with solution-based
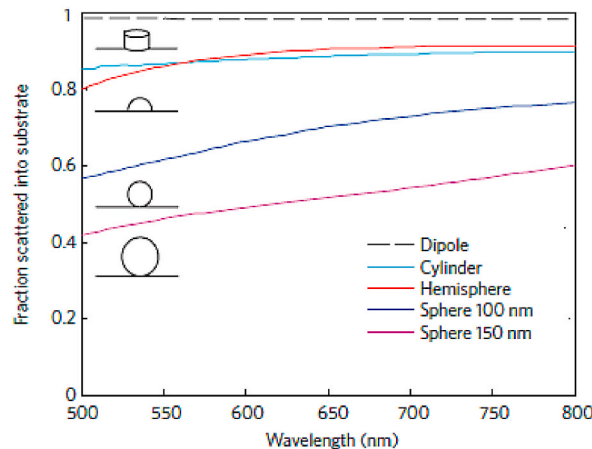

Fig. 5. The effect of Ag NPs size and shape on light scattering [58].

device processing. Optimizing the use of this effect requires the absorption rate of the active layer materials to be greater than the reciprocal of the decay time of the plasmon [58]. This prevents the dissipation of absorbed solar energy by ohmic damping. Nonetheless, the MNPs can also jeopardize the carrier mobility of the active layer thus counteract the benefits of near-field effect [63]. It is therefore imperative to carefully choose the NPs size, shape, and position such that the optoelectronic benefits accrued from the near-field effect out ways the adverse effects of degraded carrier mobility and light absorption by the MNPs. Nonetheless, the light trapping of the near-field effect has been shown to out way light absorption of the MNPs in PSCs [64]. Further, the MNPs can be coupled with high carrier mobility GNMs to simultaneously improve charge transport in the solar cells.

MNPs promote light energy conversion through plasmon-induced charge separation. This results from excitation of electron-hole pairs of the metals through interband and intraband transitions that cause transfer of energy to the primary hot charge carriers [65,66]. The hot electrons thereby multiply through electron-electron scattering accompanied by energy redistribution typical of Fermi-Dirac distribution [67–69]. The timescale for the e-e scattering is a few hundreds of femtoseconds while that for the energy redistribution is from few hundreds of femtoseconds to picoseconds. Of these processes, plasmon-induced charge separation takes relatively longer time due to the secondary excitation of electron-hole pairs [55]. The hot electron transfer is usually manifested in n-type semiconductor (e. g. TiO_2)-MNPs Schottky barrier. This gives rise to a charge separation between the conduction band of the semiconductor and the metal resulting in light energy conversion [66,70]. The interband and intraband transition of electrons get injected from the MNPs to the conduction band of the semiconductor *via* tunnelling or overcoming the Schottky barrier. The exquisite feature of this approach is in harvesting of energy of the electrons ejected from the MNPs thus, circumventing band-gap limitation to energy absorption of the semiconductor [55]. Thus, the charge separation results from primary and secondary excitation of electron-hole pairs *via* Landau damping and e-e scattering, respectively. Plasmon-induced charge separation is usually observed in PSCs when a HTL is deposited on an n-type semiconductor loaded with MNPs.

Silver sulphide NPs prepared by wet chemical method was employed in the active layer of inverted poly 3-hexylthiophene (P3HT) [6,6]:-phenyl-C_{61}-butyric acid methyl ester ($PC_{61}BM$) based solar cells [72]. At an optimum concentration of Ag_2S, the devices produced a PCE of 5.15% which was a significant improvement in comparison to the reference device with a PCE of 2.33%. The devices manifested improved optical absorption and electrical properties. This was attributed to excitation of SPPs and light scattering in the photoactive medium by Ag_2S NPs. Similarly, ZnS NPs employed in the photoactive medium of P3HT:PCBM based solar cells improved the PCE from 1.9 % in the reference device to 4 % at the optimum concentration of the NPs [73]. The improved performance accrued from the creation of a near-field along the MNPs thereby promoting charge separation and transport. Also, ZnS in the active layer produced a light scattering effect which improved photon harvesting.

Poly[[2,5- bis(2- hexyldecyl-2,3,5,6- tetrahydro-3,6-dioxopyrrolo[3,4-*c*]pyrrole- 1,4- diyl]- *alt*- [3′,3″-dimethyl-2,2′:5′,2″- terthiophene]- 5,5″- diyl] (PMDPP3T):$PC_{71}BM$ solar cells were fabricated with Ag and Au nanostars in the active layer [74]. A maximum J_{sc} of 21.58 and 23.39 mA cm^{-2} was achieved in the devices with Au and Ag nanostars, respectively. This was an improvement in comparison to the reference device with a maximum J_{sc} of 19.6 mA cm^{-2}. The improved J_{sc} was attributed to enhanced light absorption. The nanostars effected in-plane light scattering in the active layer which increased the optical path length thereby promoting light absorption. Poly{[4,8-bis-(2-ethyl-hexyl-thiophene-5-yl)-benzo[1,2-b:4,5-b′]dithiophene-2,6-diyl]-alt-[2-(2′-ethyl-hexanoyl)-thieno [3,4-b]thi-ophen-4,6-diyl]}(PBDTTT-C-T): $PC_{71}BM$ were fabricated with Ag NPs in the HTL and active layer [75]. The devices with Ag NPs in both the HTL and active layer realized better $J_{sc,}$ FF and PCE of 21.3 mA cm^{-2}, 55% and 9.2%, respectively. Devices with Ag NPs in the active layer yielded $J_{sc,}$ FF and PCE of 20 mA cm^{-2}, 55% and 8.41%, respectively, while the device with Ag NPs in the HTL yielded $J_{sc,}$ FF and PCE of 20.6 mA cm^{-2}, 52% and 8.26%, respectively. The reference device realized $J_{sc,}$ FF and PCE of 19.5 mA cm^{-2}, 52% and 7.56%, respectively. The enhanced J_{sc} and FF was attributed to enhanced broadband absorption and good charge transport, respectively. The optimized size for the NPs for HTL was 20 nm whilst for active layer was 7 nm. This study reveals that simultaneous application of MNPs in the interfacial and active layers of PSCs yields better performance than in either of the layers.

Silver doped nickel oxide nanocomposite prepared by thermal decomposition was employed in the photoactive medium of P3HT: PCBM-based solar cells [76]. The nanocomposite improved photon absorption and exciton generation and dissociation of the devices
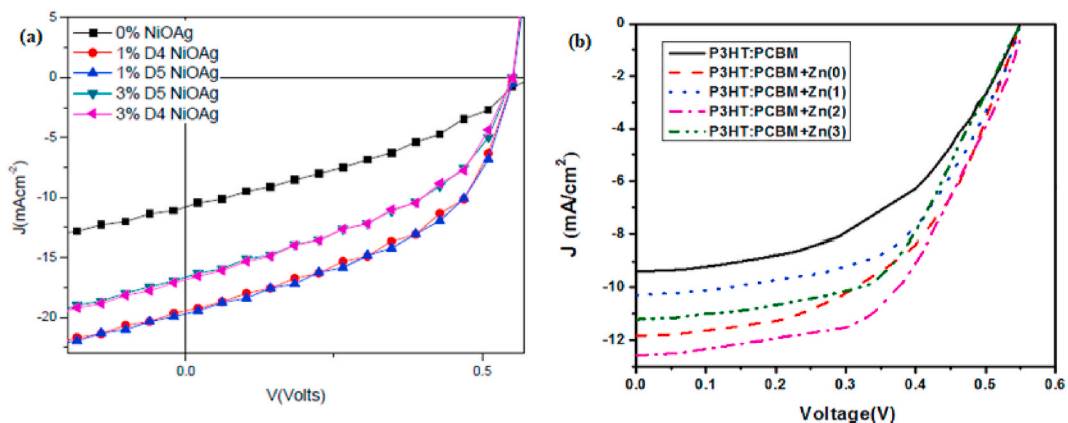

Fig. 6. J_{sc} of P3HT:PCBM-based solar cells with (a) silver doped nickel oxide [76] and (b) zinc doped tin sulphide in the active layer [77].

through near-field effect to yield enhanced J_{sc} (as shown in Fig. 6a) and PCE. The J_{sc} and PCE improved from 8.91 mA cm^{-2} to 2.01% to 19.63 mA cm^{-2} and 5.13%, respectively. Zinc doped and undoped tin sulphide NPs synthesized by ultrasound method were incorporated in the active layer of P3HT:PCBM-solar cells [77]. In comparison to the reference device (without NPs in the active layer), the devices exhibited improved J_{sc} as shown in Fig. 6b and PCE. The devices with doped SnS and un doped SnS yielded a J_{sc}, V_{oc}, FF and PCE of 12.65 mA cm^{-2}, 0.55 V, 54% and 3.75%, and 11.84 mA cm^{-2}, 0.55 V, 55% and 3.58%, respectively. The reference device realized a J_{sc}, V_{oc}, FF and PCE of 9.4 mA cm^{-2}, 0.55 V, 48% and 2.49%, respectively. The improved performance was attributed to improved light absorption and reduced band gap and strain of the active layer that resulted in enhanced exciton generation and charge transfer. The NPs also increased carrier concentration of the active layer.

Omrani et al. [78] investigated the effect of hybrid plasmonic nanoparticles (HNPs) *viz.* SiO$_2$@Ag@SiO$_2$ on the optical-electrical performance of P3HT:PCBM solar cells. The HNPs were capped by a 1 nm SiO$_2$ layer. Typically, the capping layer should be thin to allow for the penetration of hot electrons across the Schottky barrier (caused by the layer itself) at the Ag/active layer interface. Spherically and cubic shaped HNPs were prepared by electroless pre-treatment deposition and Stober methods. The HNPs incorporated in the active layer effected optical absorption to longer wavelengths, as shown in Fig. 7a, which translated to enhanced J_{sc} (Fig. 7b) through exciton generation. The HNPs in the active layer improved optical absorption *via* high light trapping, high light scattering, interparticle hotspots and strong near-field. The optical absorption of the cubic HNPs active layer was slightly lower than that for spherical HNPs active layer. This underscores the influence of NPs shape on the photon harvesting by LSPR effect. Consequently, the devices' PCEs were improved from 3.47 to 6.75 and 6.50 %, for the spherical and cubic HNPS, respectively. Further, the study showed that the HNPs in the polymer band gap act as dopant states which provide hopping sites for hole transport thus increasing hole mobility. Similarly, hot electrons produced by the HNPs fill the trap states of the polymer active layer, thus improving electron mobility. Typically, the interactions between the inner and outer surface plasmons in HNPs give rise to enhanced LSRP properties by the reduction of the metallic shell thickness while boosting the plasmon interactions. Table 2 shows photovoltaic performance of conventional PSCs with MNPs in the active layer. It can be observed from the Table that nanorods (NRs) perform better than cubic or triangular-shaped MNPs. Similarly, polymer:MNPs only active layer device yield poor V_{oc}, J_{sc} and PCE, thus MNPs are not suitable acceptor layer materials for PSCs.

4.1.2. Interfacial layers

Different approaches are used in the integration of MNPs into the interfacial layers. MNPs can be placed in the ETL (HTL) or at the ETL (HTL) -active layer interface. This helps to mitigate the charge carrier recombination that occurs when the MNPs are placed within the active layer. In both cases, transfer of the near-field energy of the MNPs to the active layer, and light scattering results in enhanced photon harvesting and charge carriers' generation. MNPs used as optical spacers in the ETL cause maximum light intensity to fall within the photoactive medium by far-field scattering thereby improving light harvesting of the device [88]. The optical spacers also enhance the electrical properties of the devices by improving charge extraction whilst reducing the potential barrier height and charge recombination.

Dkhil et al. [89] studied the effect of insertion of solution-processed ZnO optical spacer in P3HT:PC$_{61}$BM and poly[[4,8-bis [(2-ethylhexyl)oxy] benzo[1,2-b:4,5-b′]dithiophene-2,6diyl] [3-fl uoro-2-[(2-ethylhexyl)carbonyl] thieno [3,4-b]thiophenediyl]] (PTB7): PC$_{71}$BM based solar cells. The ZnO optical spacer enhanced all the electrical parameters of the solar cells. The ZnO layer improved charge extraction and lifetime at the cathode-active layer interface. This produced enhanced J_{sc} even without an improvement in the optical absorption in the photoactive medium. Further, they showed that surfactant treated ZnO (ZnO $_{EA}$) produced smooth morphology which translated to higher FF and overall better device performance than the untreated one. This study revealed that insertion of optical spacer in PSCs not only improves light absorption of the active layer but also improves the electrical properties at the interface thus facilitating charge extraction.

Notarianni et al. [90] fabricated P3HT:PCBM based PSCs with Au NPs of different layer thickness on the ITO substrate. For a
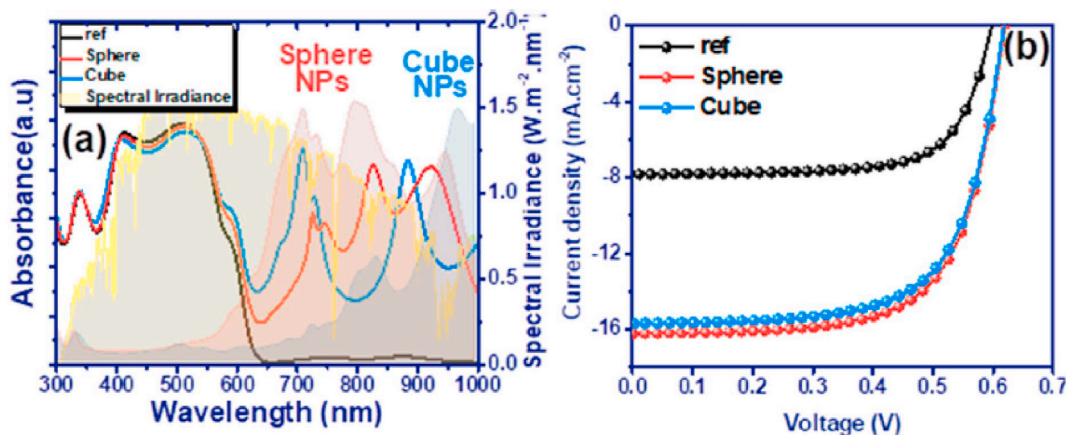

Fig. 7. (a) Optical absorption and (b) *J-V* characteristics of P3HT:PCBM active layer incorporated with spherical and cubic SiO$_2$@Ag@SiO$_2$ [78].

Table 2
Photovoltaic performance of PSCs with MNPs in the active layer.

Active layer material	V_{oc} (volts)	J_{sc} (mA cm^{-2})	FF (%)	PCE (%)	Ref
p-DTS(FBTTh$_2$)$_2$: PC$_{70}$BM: AuNR	0.78	12.58	70	6.9	[79]
p-DTS(FBTTh$_2$)$_2$:PC70BM:Au–SiO$_2$NR	0.77	15.40	70	8.2	[79]
P3HT:PC$_{61}$BM:AuRD	0.61	10.39	65	4.14	[80]
P3HT:PC$_{61}$BM:Au cube	0.60	9.95	63	3.75	[80]
P3HT:PC$_{61}$BM:Au triangle	0.60	9.57	63	3.62	[80]
P3HT:PC$_{61}$BM:Ag:Cu	0.57	11.40	53	4.7	[81]
P3HT:PCBM:Ag@SiO$_2$	0.61	9.72	67	3.94	[82]
P3HT:PC$_{61}$BM:ZnO	0.57	7.27	46	1.91	[83]
P3HT:PCBM:ZnO NW + NP	0.57	11.8	57	4.10	[84]
P3HT-CuO	0.39	2.18	54	0.47	[85]
P3HT-CuO:Fe	0.36	2.01	56	0.41	[85]
P3HT:PCBM:CuO	0.67	6.48	68	2.96	[86]
P3HT:PC$_{70}$BM:CuO	**0.61**	**9.14**	**67**	**3.70**	[87]

different shape, a 1 nm layer was deposited through a mask of Au. The J_{sc} of the devices with Au NPs increased with decreasing layer thickness to a maximum value of 9.9 mA cm^{-2} with a PCE of 3.64% at the lowest thickness deposited through a mask. This was a slightly improved performance in comparison to the reference device with J_{sc} of 9.45 mA cm^{-2} and PCE of 3.35%. The mask increased the distance between the NPs, reducing reflection whilst increasing the forward scattering of light for enhanced performance. This study reveals the effect of distance and MNP size on the performance of PSCs, i.e., NPs of thin layers yield better performance.

Hybrids of Au–Ag NPs were employed in the PEDOT: PSS HTL of P3HT: PC$_{61}$BM-based solar cells [91]. At an optimum concentration of the NPs hybrid in the HTL, a J_{sc}, V_{oc}, FF and PCE of 12.87 mA cm^{-2}, 0.54 V, 58% and 4.03%, respectively, was realized. This was an improved performance in comparison to the P3HT: PC$_{61}$BM reference device with PEDOT: PSS HTL, which exhibited a J_{sc}, V_{oc}, FF and PCE of 10.6 mA cm^{-}2, 0.57 V, 55% and 3.3%, respectively. The enhanced performance originated from improved light absorbance due to light scattering caused by the NPs. Also, the hybrid NPs modified HTL devices outperformed those modified by either Au NPs or Ag NPs. PEDOT: PSS + Ag NPS and PEDOT: PSS + Au NPS HTL devices yielded a PCE of 3.45 and 3.96%, respectively. Hence, this study reveals that the utilization of MNP hybrids is yet another strategy in the optimization of device performance. The study further revealed that small-sized NPs do not adversely affect the morphology of the HTL.

4.2. Application of hybrids of metallic nanoparticles/graphene nanomaterials in polymer solar cells

Given the outstanding properties of graphene and MNPs, as discussed in sections (1) and (2), a nanocomposite of these materials would possess unique properties arising from the atomic-scale mixing of the component's properties. For example, synergy in the high carrier mobility and specific surface area of graphene and the high optical absorption of MNPs would yield a nanocomposite characterized by high optical absorption and charge carrier mobility. Thus, such a hybrid nanomaterial is suitable for enhancing the performance of PSCs. Nonetheless, interaction between the GNMs and MNPs at the graphene-metallic interface is crucial in tailoring the physico-chemical properties of the nanocomposite. For example, the electronic property of graphene is influenced by the interaction with metallic atoms [4]. These nanocomposites can be utilized in the active and interfacial layers of PSCs.

4.2.1. Interfacial layers

GO sheets decorated with Au NPs and Au NRs were used as HTL in PTB7:PCBM solar cells [92]. As shown in Table 3, the nanocomposite-modified devices realized significant improvement in the electrical parameters to yield improved PCE compared to GO HTL device. The Au NPs were of different sizes, i.e. NPs 1, 2 and 3 measured 5, 20 and 40 nm, respectively, while the NRs measured 40 nm in length and 15 nm in diameter. The improved V_{oc} in the NP devices was attributed to complete coverage of the ITO substrate. Conversely, the reduced V_{oc} in the NRs device was due to inhomogeneous morphology caused by incomplete coverage of the substrates. The improved J_{sc} values in all the devices with Au nanostructures (NSs) originated from the light trapping effect of the plasmonic structures. This work demonstrated the impact of size and shape of the plasmonic NPs on light harvesting, whereby the devices' optical absorption increased with decreased NP size while the NRs manifested the best absorption. This corroborated with the J_{sc} values. The improved FF in the nanocomposite modified devices was attributed to reduced resistivity at the HTL-active layer interface, leading to effective charge extraction to the anode.

Table 3
Electrical parameters of PTB7:PCBM solar cells with GO: Au NSs as HTL [92].

HTL material	V_{oc} (volts)	J_{sc} (mA cm^{-2})	FF (%)	PCE (%)
GO	0.74	10.51	52	4.11
GO: Au NP1	0.78	12.04	59	5.5
GO: Au NP2	0.75	11.55	68	5.88
GO: Au NP 3	0.73	11.50	61	5.10
GO: Au NR	**0.65**	**12.83**	**57**	**4.80**

Gollu et al. [93] fabricated inverted P3HT:PCBM solar cells with rGO/ZnO as the ETL. As shown in Fig. 8a, the optimum concentration of rGO in the rGO/ZnO ETL devices led to improved J_{sc} values. The optimal rGO concentration *viz.* 0.4 mg/mL in the ETL resulted in a J_{sc}, V_{oc}, FF and PCE of 9.46 mA cm^{-2}, 0.63 V, 64% and 3.81%, respectively. This was a slightly improved performance compared to ZnO ETL device, which yielded a J_{sc}, V_{oc}, FF and PCE of 0.61 V, 8.05 mA cm^{-2}, 63% and 3.13%, respectively. The improved performance was attributed to reduced charge recombination, thus better electron collection efficiency effected by rGO. With the optimum rGO concentration in rGO/ZnO ETL, the group fabricated devices with Au and Ag NPs/NRs in the active layer. The average diameter of the spherically shaped NPs was 50 nm, while the NR's average length and width were 50 nm and 10 nm, respectively. The Au and Ag NSs in the active layer gave rise to improved J_{sc} and PCE with a maximum of 12.21 mA cm^{-2} and 4.85%, respectively, in comparison to P3HT: PCBM only devices with J_{sc} and PCE of 9.49 mA cm^{-2} and 3.77%, respectively (Fig. 8b). Further, they performed Mie scattering calculations for the system of P3HT: PCBM embedded with either Au or Ag NSs using the finite difference time domain (FDTD) simulation technique to elucidate the light absorption mechanism of the active layer. They observed near-field enhancement from LSPR at the NSs/active layer interfaces. This gave rise to increased optical absorption of the active layer. The maximum scattering cross-section for the NPs and NRs occurred in the wavelength range of 400–650 nm and 450–650 nm, respectively. Overall, the absorption and scattering cross-sections of the NRs were larger than for the NPs, leading to better light absorption in the former. This resulted in better J_{sc} and PCEs in the NRs devices than those with NPs. The NSs in the active layer also improved charge transport with the best carrier mobility, μ of $4.64 \times 10^{-3}\ cm^3V^{-1}s^{-1}$ exhibited by device with Au NRs while the P3HT: PCBM only device exhibited μ of $3.36 \times 10^{-3}\ cm^3V^{-1}s^{-1}$. This study underscores the effect of the metallic plasmonics size and shape on the optical absorption and charge transfer in PSCs. It also shows that simultaneous use of hybrids of MNPs/GNMs in the interfacial layer and MNPs in the active layer of PSCs remarkabky improves the device performance because of the synergistic effect of the material's properties.

4.2.2. Active layer

ZnO decorated graphene nanocomposite (Z@G) was synthesized by microwave-assisted hydrothermal process and employed in the active layer of PSCs with the architecture of ITO/PEDOT: PSS/PCPDTBT:PCBM: Z@G/Al [94]. The devices realized a J_{sc}, V_{oc}, FF and PCE of 17.45 mA cm^{-2}, 0.66 V, 32% and 3.65%, respectively. This was an improvement compared to ZnO modified active layer device with a J_{sc}, V_{oc}, FF and PCE of, 9.53 mA cm^{-2}, 0.59 V, 31% and 1.76%. The significant enhancement in J_{sc} was attributed to the uniform flake-shaped structure of the active layer film formed with the Z@G. This unique pattern originated from the hybridization of C-60 compound and graphene sheet, favouring charge carrier transportation, thus suppressing charge carrier losses. It should be noted that there is not much literature on the use of hybrids of MNPs and GNMs in the active layer of PSCs.

As aforementioned, the size, shape and composition of the MNPs influence their performance in PSCs. Small-sized MNPs yield better PCE through enhanced optical absorption by forward light scattering and better morphology when incorporated in the active or interfacial layers. On the other hand, large-sized MNPs promote backscattering, which doesn't necessarily yield better optical absorption. Similarly, improvement in light harvesting by near-field effect is more pronounced in small-sized MNPs. During device fabrication, it is easier to achieve a homogenous active layer solution, yielding a good film morphology with small-sized MNPs than large ones. A good film morphology implies better charge transport because of reduced charge recombination centres. The shape and structure of the MNPs directly influence their plasmonic effect in PSCs. For example, spherical-shaped MNPs yield better light absorption than cube-shaped ones. Similarly, a core-shell structure of the MNPs delivers good performance provided that the capping layer is kept low to avoid minimizing the benefits of the near-field effect. Using hybrids of different MNPs has a better impact on PCE than the individual components because of the synergistic LSPR effect, yielding better light absorption. The simultaneous use of the hybrids of MNPs/GNMs and MNPs in the interfacial and active layers of PSCs improves the devices' light harvesting and charge transport, which translates to enhanced PCE.
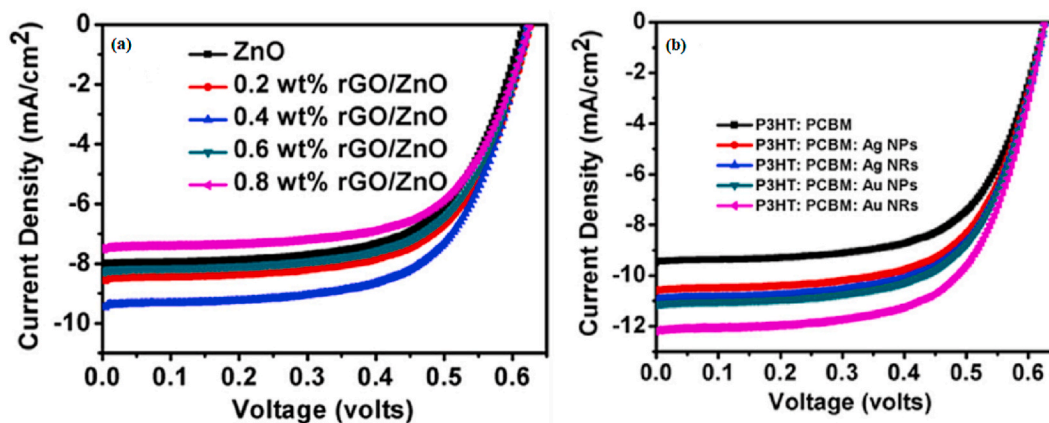

Fig. 8. J_{sc} of (a) rGO/ZnO ETL and P3HT:PCBM solar cells (b) rGO/ZnO ETL and P3HT:PCBM: Ag(Au) solar cells [93].

5. 5.Application of metallic nanoparticles and hybrids of metallic nanoparticles/graphene nanomaterials in dye sensitized solar cells

DSSCs are one of the most promising low-cost solar energy conversion technologies. As shown in Fig. 9, DSSCs comprise five main parts. A transparent conductive oxide (TCO), usually of fluorine-doped tin oxide (FTO) which serves as the cathode, a dye which is the light absorber, a photoanode which is made of a wide band gap semiconductor like mesoporous TiO_2; this serves as a support for loading of dye and the medium for electron transport, an electrolyte of redox couple such as iodide/triiodide, and a counter electrode (CE) usually made of platinum. Upon solar irradiation, the dye molecules absorb photons and generate electron-hole pairs. Charge separation occurs at the dye-TiO_2 interface. This is followed by the transfer of the photoexcited electrons to the conduction band of the semiconductor and the subsequent transportation of the electrons to the cathode. The electrolyte transports the hole from the dye (regenerates the dye) to the counter electrode. Meanwhile, the electrons from the external circuit get to the CE and regenerate the electrolyte. The CE catalyses the reduction reaction of the redox couple. Thus, it should be characterized by high catalytic activity and surface area. A major drawback to high efficiencies in DSSCs is charge carrier recombination in the photoanode. Hence, the photoanode material should have a high electron mobility. Standard dyes like N719, N19, N3, and N749 absorb light in the 300–700 nm wavelength range [95]. Broadening of absorption wavelength of the natural dyes can be achieved by using co-sensitizers with different spectral responses [96]. MNPs have shown potency in increasing the sensitizer's molar absorption coefficient. MNPs used as photoanode additives enhance light absorption through LSPR. This allows for the reduction of TiO_2 thickness without compromising light absorption. A thin TiO_2 layer implies reduced travel distance of charges to the external circuit, thus reduced charge recombination. GNMs incorporated in the photoanode create charge percolation pathways for electron transport and increase the surface area of TiO_2 for dye loading. Therefore, hybrids of MNPs and GNMs used as photoanode additives would synergistically enhance light absorption and electron transport for high photovoltaic performance. Similarly, owing to the high surface area and electrical conductivity of GNMs, and the high catalytic activity of MNPs, hybrids of these nanomaterials in the CE would yield high electocatalytic activity.

5.1. Application of metallic nanoparticles in dye sensitized solar cells

5.1.1. Photoanode additive
Bhullar et al. [97] fabricated DSSCs with Ag ion implanted TiO_2 NPs-(nanofibers)NFs photoanode. Typically, TiO_2 NFs are characterized by low number of grain boundaries and thus exhibit better charge transport. Nonetheless, the NFs, given their low surface area to volume ratio (because of their 1D nature) would result in low dye loading. In preparation of the photoanodes, TiO_2 NFs were mixed in TiO_2 NPs at a ratio of 3:7 to rip the benefits of the different NSs. This was followed by implanting Ag ion beams at different fluences. It was observed that substitutional and interstitial Ag doping occurred at lower and higher Ag fluence, respectively. At optimum Ag fluence, the photoanode-modified device yielded a J_{sc}, V_{oc}, FF and PCE of 13.93 mA cm^{-2}, 0.74 V, 73% and 7.47%, respectively. On the other hand, the device with TiO_2 NPs-NFs only photoanode realized a J_{sc}, V_{oc}, FF and PCE of 13.36 mA cm^{-2}, 0.72 V, 61% and 6.13%, respectively. The enhanced performance after Ag implantation was attributed to hot electron generation and the creation of electron states beneath the conduction band of TiO_2. Also, the inclusion of Ag promotes charge separation at the photoanode/electrolyte interface thus, limits charge carrier recombination. The Ag implanted photoanode devices manifested the maximum electron lifetime *ca* 21.75 ms compared to the TiO_2 NPs-NFs device with 9 ms, implying reduced charge recombination. However, beyond the optimum Ag fluence, the photovoltaic performance decreased due to low dye loading and a higher band gap originating from distorted TiO_2 film. Using Density Functional Theory (DFT) simulations, it was observed that new impurity levels, a decrease in TiO_2 band gap and an upward shift in Fermi level occurred with substitutional Ag doping. These resulted in improved light absorption and increased V_{oc}. Further, the ion implantation method produced a protective layer over the Ag atoms, increasing device stability.

Multi-shaped (spherical, oval, rods and triangle) Ag NPs prepared by chemical reduction method and incorporated in the TiO_2
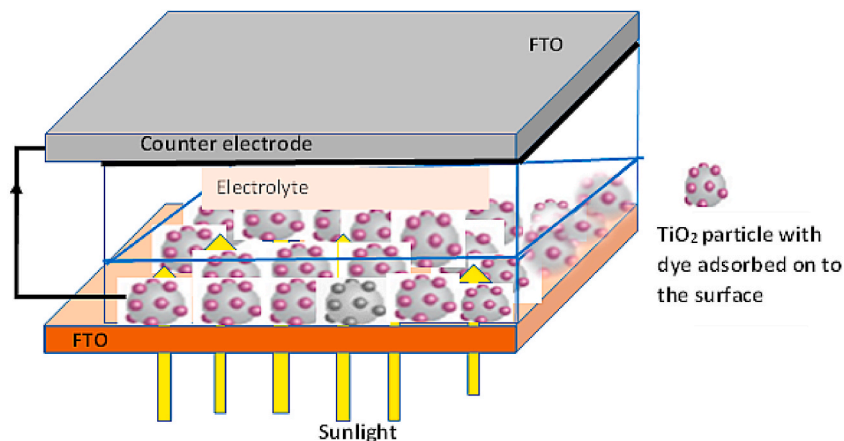

Fig. 9. Schematic diagram of DSSC.

photoanode resulted in improved photovoltaic performance of N719 DSSCs [98]. The best-performing device (with uniform spherical-, triangle- and rod-shaped Ag) realized a J_{sc}, V_{oc}, FF and PCE of 15.75 mA cm^{-2}, 0.77 V, 63% and 7.64%, respectively, compared to the bare TiO$_2$ device with a J_{sc}, V_{oc}, FF and PCE of 10.51 mA cm^{-2}, 0.74 V, 68% and 5.28%, respectively. The Ag NPs improved light absorption by the overlap of its SPR bands to the absorption maximum of the dye and extending the absorption wavelength of the dye. The Ag Nps in the TiO$_2$ matrix enhanced charge transport, reducing charge recombination. The increased V_{oc} was attributed to a negative potential shift of the Fermi level due to the charging of Ag/TiO$_2$. On the other hand, the increased J_{sc} was attributed to light trapping by the NPs, charge generation, separation and interfacial charge transport.

Ag NPs of size 29 nm prepared by solvothermal method were employed as a photoanode additive in N719 DSSCs [99]. The NPs were prepared at different sizes *ca.* 23, 25, 29 and 36 nm but the 29 nm sized ones exhibited the best optical absorbance and agglomeration status. At an optimum concentration of the Ag NPs, the devices realized J_{sc}, V_{oc}, FF and PCE of 10 mA cm^{-2}, 0.70 V, 67% and 4.69%, respectively. This was a better performance compared to the TiO$_2$ photoanode device with J_{sc}, V_{oc}, FF and PCE of 5.15 mA cm^{-2}, 0.75 V, 61% and 2.35%, respectively. The improved performance was attributed to improved light harvesting and electron injection by Ag NPs. However, at higher loading, Ag NPs not only sapped the LSPR effect by irregular coverage of TiO$_2$ but also formed agglomerate which acted as charge trap sites in the photoanode, thus limiting the PCE.

Layer-by-layer assembled TiO$_2$–Ag–TiO$_2$ photoanodes used in N719 DSSCs produced over 65% enhancement in PCE [100]. The plasmonic photoanode device yielded J_{sc}, V_{oc}, FF and PCE of 19.39 mA cm^{-2}, 0.82 V, 69% and 11.00%, respectively, while the TiO$_2$ device realized J_{sc}, V_{oc}, FF and PCE of 15.02 mA cm^{-2}, 0.72 V, 61% and 6.67%, respectively. The improved J_{sc} was attributed to increased dye loading, while the enhanced V_{oc} originated from a negative shift in the Fermi level occasioned by the Ag NPs. Charge carrier recombination was reduced in this device with an electron lifetime of 25.3, implying better charge collection. Further, the plasmonic photoanode device retained 91.5% of PCE after five days.

Ran et al. [101] incorporated Au and Ag NPs and nanowires (NWs) into a hybrid (2D nanosheets, 3D microspheres, 3D hollow spheres and P25 NPs) TiO$_2$ prepared by hydrothermal method to function as the photoanode of N719 DSSCs. Ag NPs and Au NPs had diameters of ~10 nm and <10 nm, respectively, while the Ag NWs and Au NWs had diameter <3 nm, length ~ 0.9–10 μm and diameter ~ 30 nm, length ~ 100–200 μm, respectively. The photovoltaic performance of devices fabricated with these photoanodes is shown in Table 4. The improved performance upon incorporating the different metal NSs was attributed to enhanced light harvesting and improved charge transport. The superior performance of Ag NWs modified photoanode originated from increased dye loading, enhanced light scattering due to its larger size and enhanced electromagnetic field. This study shows the effect of shape on the LSPR effect in DSSCs.

Salimi et al. [102] prepared mesoporous TiO$_2$ microspheres by a solvothermal treatment method and functionalized these with a primary amine (-NH$_2$) group. The microspheres were loaded with Au NPs (seed) before coating with an Ag shell to form Ag–Au@TiO$_2$ nanocomposites. This nanocomposite was used as a photoanode in N719 DSSCs, which exhibited J_{sc}, V_{oc}, FF and PCE of 17.18 mA cm^{-2}, 0.66 V, 66% and 7.41%. This was an improvement in comparison to bare TiO$_2$ and Au@TiO$_2$ photoanode devices with J_{sc}, V_{oc}, FF, and PCE of 13.41 mA cm^{-2}, 0.68 V, 65%, 5.91%, respectively, and 17.20 mA cm^{-2}, 0.64 V, 62%, 6.86%. Even though both Au@TiO$_2$ and Ag–Au@TiO$_2$ photoanodes exhibited enhanced optical absorption by LSPR effect compared to bare TiO$_2$, the intensity for the latter was greater than for the former. The enhanced optical absorption was the origin of the remarkably improved J_{sc}. Further, the accumulation of electrons around the Ag shell caused a shift in the Fermi level near the conduction band of TiO2, promoting charge separation.

Sheehan et al. [103] synthesized Au@SiO$_2$@TiO$_2$ with Au and SiO$_2$ thickness of 9 and 1.6 nm, respectively, and Au@SiO$_2$@TiO$_2$ aggregates, by simple solution-phase methods. The TiO$_2$ shell thickness was 2.5 (thin) and 7 nm (thick). The core-shell-shell NSs with different thicknesses were used as the photoanode in N719-DSSCs. The devices' performance is shown in Table 5. The enhanced performance due to thin Au@SiO$_2$@TiO$_2$ was attributed to the near-field effect owing to the proximity of TiO$_2$ to the Au core shell. On the other hand, the slightly improved performance of thick Au@SiO$_2$@TiO$_2$ was attributed to minimal far-field scattering. The highest enhancement observed for the aggregates was attributed to coupled plasmonic modes (with more prominent dipole moments), which give rise to high electromagnetic fields. The aggregates exhibited broadband absorption in the entire visible light region owing to vast interparticle distribution among the aggregated NPs. Au@Ag@Ag$_2$S NRs prepared in two steps, i.e., Au@Ag heterogenous NRs synthesized by one-pot polyol reaction followed by coating with a thin shell of Ag$_2$S was incorporated in TiO$_2$ photoanode of N719 DSSCs [104]. The NRs-modified photoanode exhibited better optical absorption in the broader wavelength range by plasmonic effects than bare TiO$_2$, leading to increased J_{sc} and PCE. The modified and bare TiO$_2$ devices showed J_{sc}, V_{oc}, and PCE of 13.21 mA cm^{-2}, 0.743 V, 6.51% and 10.18 mA cm^{-2}, 0.717 V, 4.65%, respectively. The slight enhancement of V_{oc} was attributed to the up-shift of the conduction band of TiO$_2$.

Glutathione-capped gold nanoclusters (NCs) Au$_x$-GSH NCs, with metal core and thiolated shell, utilized as cosensitizers in N719

Table 4
Electrical parameters of N719-based DSSSs with Au and Ag NPs and NWs modified photoanode [101].

Photoanode	V_{oc} (volts)	J_{sc} (mA cm^{-2})	FF (%)	PCE (%)	Dye loading ($\times 10^{-7}$ mol cm^{-2})
TiO$_2$	0.70	11.83	72	4.58	1.86
Au NP- TiO$_2$	0.67	10.65	67	4.76	1.98
Ag NP-TiO$_2$	0.67	10.74	67	4.81	1.99
Au NW- TiO$_2$	0.65	12.12	64	5.10	1.98
Ag NW- TiO$_2$	**0.68**	**13.02**	**65**	**5.74**	**3.25**

Table 5
Electrical parameters of DSSCs with Au@SiO$_2$@TiO$_2$ photoanode [103].

Photoanode Nanostructures	V_{oc} (volts)	J_{sc} (mA cm^{-2})	FF (%)	PCE (%)
None	0.75	6.64	57	2.81
Ag@SiO$_2$ (1.6 nm)	0.75	7.78	60	3.52
Au@SiO$_2$@TiO$_2$ (4.1 nm)	0.77	9.37	57	4.02
Au@SiO$_2$@TiO$_2$ (8.6 nm)	0.75	6.81	58	2.99
Aggregates	**0.80**	**11.59**	**59**	**5.52**

and squaraine (SQ) DSSCs resulted in improved photovoltaic performance [105]. The cosensitized SQ and N719 DSSCs realized a J_{sc}, V_{oc}, FF and PCE of 6.7 mA cm^{-2}, 0.9 V, 66% and 4.0% and 5.34 mA cm^{-2}, 0.87 V, 69% and 3.2%, respectively. On the other hand, DSSCs with SQ and N719 single sensitizers yielded a J_{sc}, V_{oc}, FF and PCE of 5.12 mA cm^{-2}, 0.66 V, 70% and 2.4% and 5.24 mA cm^{-2}, 0.73 V, 52% and 2.0%, respectively. The improved performances accrued from complementary optical absorption of the two sensitizers in the visible region and suppressed back electron transfer. Incident photon to current conversion efficiency (IPCE) measurement for SQ dye and NCs cosensitized device showed a photoresponse in the red (550–800 nm) and blue (below 500 nm) regions of the solar spectrum. The high values of V_{oc} originated from accumulation of electrons (because of suppressed back electron transfer) at the TiO$_2$ photoelectrode which shifts the Fermi level to more negative potentials. Also, the metal core accepts and stores electrons (behaves as a nanocapacitor), thus maintaining a more negative Fermi level at the TiO$_2$ photoanode.

Hierarchical structured TiO$_2$ synthesized by hydrothermal route were employed as photoanodes in N719-based DSSCs [106]. This study showed the influence of growth time on the TiO$_2$ morphology whereby nanorods and microflowers (composed of numerous nanothorns) were obtained at 12 and 18 h growth duration, respectively. When utilized as a photoanode, the microflowered TiO$_2$ exhibited better electrical parameters and PCE *ca.* 1.2% than the nanorod with PCE of 0.51%. The numerous open structured nanothorns in the microflowered morphology TiO$_2$ enhanced dye adsorption and thus light harvesting. In another study, N719 DSSCs fabricated with spherically shaped Mn–TiO$_2$ NPs, prepared by hydrothermal method, as photoanode produced J_{sc}, V_{oc}, FF and PCE of 5.56 mA cm^{-2}, 0.64 V, 66% and 1.84%, respectively [107]. This was an inferior performance compared to bare TiO$_2$ photoanode device, which exhibited a J_{sc}, V_{oc}, FF and PCE of 8.72 mA cm^{-2}, 0.71 V, 75% and 5.27%, respectively. The inferior performance was attributed to charge recombination and reduced charge collection.

Ag/La$_{0.6}$Sr$_{0.4}$CoO$_3$ nanoparticles were used as a photoanode additive in N719 DSSCs [108]. The La$_{0.6}$Sr$_{0.4}$CoO$_3$ perovskite NPs were first prepared by sol-gel method followed by Ag loading by solution phase method. The Ag NPs were observed to be of spherical shape. The plasmonic photoanode exhibited superior performance with J_{sc}, V_{oc}, FF and PCE of 17.32 mA cm^{-2}, 0.75 V, 46% and 6.04%, respectively, while TiO$_2$ photoanode yielded J_{sc}, V_{oc}, FF and PCE of 10.54 mA cm^{-2}, 0.69 V, 42% and 3.04%, respectively. The significantly improved performance was attributed to enhanced optical absorption, charge transport and charge separation. The Ag NPs and the porous nature and high surface area of La$_{0.6}$Sr$_{0.4}$CoO$_3$ NPs promoted dye loading, increasing light harvesting. Also, Ag NPs improved light absorption by the LSPR effect. Electron lifetime was observed to be longest in Ag/La$_{0.6}$Sr$_{0.4}$CoO$_3$ photoanode devices, implying reduced charge recombination because of better charge transport.

Table 6
Electrical parameters of N719 DSSCs with various MNPs modified photoanode.

Photoanode material	Method	V_{oc} (volts)	J_{oc} (mA cm^{-2})	FF (%)	PCE (%)	Ref
TiO$_2$+Au@SiO$_2$ (spherical)	Chemical reduction and hydrolysis	0.73	20.31	69	10.21	[109]
TiO$_2$+Au@TiO$_2$ (spherical)	Chemical reduction and hydrolysis	0.77	18.28	69	9.78	[109]
TiO$_2$+Au@SiO$_2$ (spherical)	Turkevish	0.72	13.28	60	5.74	[110]
TiO$_2$+Au NPs (spherical)	Turkevish	0.72	6.41	57	2.3	[110]
Au@TiO$_2$ (octahedral)	Solution phase synthesis	0.72	14.75	70	7.30	[111]
SWNTs@(TiO$_2$/Ag/Au) (wire-like)	Solution phase synthesis	0.72	16.80	70	8.30	[112]
SWNTs@(TiO$_2$/Ag) wire-like	Solution phase synthesis	0.72	15.40	70	7.80	[112]
Ag@TiO$_2$ (spherical)	Sol gel	0.75	18.70	64	8.90	[113]
Ag@TiO$_2$ (spherical)	Sol process	0.74	8.93	59	5.00	[114]
Ag–TiO$_2$ (cube)	Hydrothermal	0.67	17.20	57	6.44	[115]
Ag–TiO$_2$ (nanorods)	Green synthesis	0.67	14.20	67	6.42	[116]
Au–TiO$_2$ (spherical)	Turkevish	0.61	9.81	45	2.72	[117]
Ag/AgBr/TiO$_2$ (varied shapes)	Sol-gel	0.71	18.78	63	8.46	[118]
Ag–TiO$_2$ (cauliflower)-	Hydrothermal	0.77	10.80	50	4.15	[119]
Ag–TiO$_2$ (not well defined)	Green synthesis	0.69	11.00	48	4.09	[120]
Au–TiO$_2$–Ag (spherical)	Electro-hydrodynamic	0.74	15.20	63	7.51	[121]
Au–Ag NPs/TiO$_2$ (spherical)	Pulsed laser ablation	0.76	11.67	65	5.81	[122]
Ag–TiO$_2$ nanospheres	Sol-gel	0.69	11.90	64	5.24	[123]
TiO$_2$–Ag nanowires	Hydrothermal	0.68	13.02	65	5.74	
TiO$_2$–Ag NPs (spherical)	Chemical reduction	0.67	18.13	66	8.39	[124]
TiO2+Ag nanoplate (triangular)	**Solution phase**	**0.70**	**12.47**	**44**	**3.84**	[125]

@refers to core-shell structured MNPs.

The photovoltaic performance of DSSCs with TiO_2 photoanode modified by various MNPs is shown in Table 6. This Table underscores the influence of MNPs' composition, shape and preparation method on the photovoltaic performance of plasmonic DSSCs. For example, photoanodes of spherically shaped $TiO_2+Au@SiO_2$ prepared by the chemical reduction method perform better than those produced by Turkevish, i.e., holding other factors constant. Similarly, nanowire-shaped Ag–TiO_2 photoanodes performs better than cauliflower-shaped ones even though both are prepared by the hydrothermal method. Doctor blade, screen printing, drop casting, spin coating ion implantation and laser ablation are the commonly used techniques for photoanode preparation. Of these, the doctor blade is the most widely used method.

5.1.2. Counter eletrode

$ZnO@WO_3$ core-shell nanoparticles (shown in Fig. 10 a) were synthesized by sol-gel method and drop cast on ITO substrate to form CE in DSSCs [126]. The WO_3 shell reduced the energy band gap of ZnO. Also, the $ZnO@WO_3$ exhibited decreased photoluminescence emission attributed to photogenerated charge carrier separation. As shown in Fig. 10b, the DSSCs with $ZnO@WO_3$ as CE exhibited higher J_{sc} and better performance *ca.* J_{sc}, V_{oc}, FF and PCE of 12.1 mA cm^{-2}, 0.89 V, 60% and 5.73%, respectively, than the Pt device *ca.* J_{sc}, V_{oc}, FF and PCE of 11.4 mA cm^{-2}, 0.62 V, 52% and 4.51%. The improvement in FF and V_{oc} was attributed to higher electrical conductivity, while the enhanced J_{sc} was attributed to better light harvesting by the photoanodes stacked on the $ZnO@WO_3$ CE. Similarly, the $ZnO@WO_3$ and Pt devices exhibited charge transfer resistance (R_{ct}) values of 18.56 and 30.05 Ω, respectively, implying a better electrocatalytic activity by the plasmonic CE. This study heightens the potential of plasmonic electrodes for DSSCs, given the better performance of Pt CE.

5.2. Application of hybrids of metallic nanoparticles/graphene nanomaterials in dye sensitized solar cells

5.2.1. Photoanode additive

Synergy in the outstanding properties of graphene and LSPR of MNPs uniquely fits the hybrids of these nanomaterials for application in DSSCs. Dhonde et al. [127] prepared Cu-doped TiO_2/graphene (CuTGR) by sol-gel assisted hydrothermal method and employed the nanocomposite in the photoanode of N719-based DSSCs. Fig. 11(a) and (b) show the *J-V* and IPCE curves of the devices, respectively. The CuTGR photoanode device realized significant improvement in the electrical parameters with a J_{sc}, V_{oc}, FF and PCE of 19.93 mA cm^{-2}, 0.75 V, 66% and 9.81%, respectively, in comparison with the TiO_2 photoanode device with J_{sc}, V_{oc}, FF and PCE of 16.60 mA cm^{-2}, 0.63 V, 65% and 6.66%. Graphene increased the surface area of TiO_2 for dye adsorption, leading to high J_{sc}, while the Cu NPs improved the V_{oc}. IPCE measurement showed high conversion efficiency for the CuTGR device in the spectrum's 400–800 nm region.

Ethylenediamine functionalized TiO_2 nanowires graphene oxide (TiO_2 NW-NH_2/GO) loaded with Ag NPs were employed as photoanodes in N719 DSSCs [128]. To prepare the nanocomposite, TiO_2 NWs were first synthesized by solvothermal method followed by solution phase functionalization by the amine and Ag loading. The diffuse reflectance spectra of the nanomaterials showed an absorption peak at 200–400 nm for the TiO_2 NWs, which was broadened to the visible region upon amine functionalization. Also, Ag loading increased the absorption in the visible region (400–650 nm) through the surface plasmon resonance effect. Calculations of dye loading for TiO_2 NW, TiO_2 NW-NH_2, TiO_2 NW-NH_2/GO and TiO_2 NW-NH_2/GO/Ag gave 0.67×10^{-7}, 1.01×10^{-7}, 1.12×10^{-7} and 1.45×10^{-7} mol cm^{-2}, respectively. The –NH_2 group was observed to promote dye anchoring on TiO_2. As shown in Table 7, the nanocomposite photoanode device exhibited superior performance to the other photoanodes. This was attributed to various factors: (i) increased light harvesting by enhanced dye loading and surface plasmon resonance effect, (ii) the presence of GO which enhanced charge transport, thus limiting charge recombination and (iii) improved charge separation. The TiO_2 NW, TiO_2 NW/GO, and TiO_2 NW-NH_2/GO/Ag photoanodes exhibited electron lifetimes of 1.32, 2.08 and 13.36 ms, respectively. Further, of all the photoanodes, TiO_2 NW-NH_2/GO/Ag exhibited the lowest R_{ct}. These imply better charge transport.
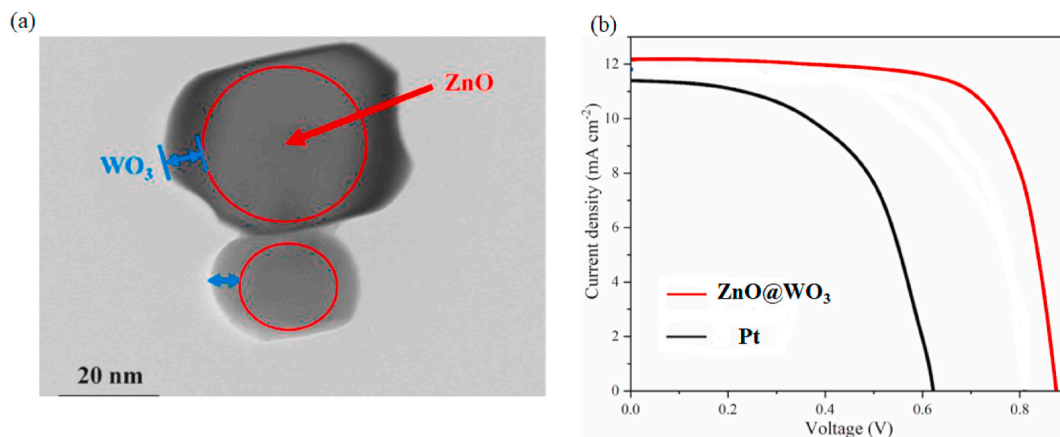

Fig. 10. (a) TEM image of $ZnO@WO_3$ nanoparticles and (b) *J-V* plot of DSSCs with $ZnO@WO_3$ and the reference counter electrode [126].
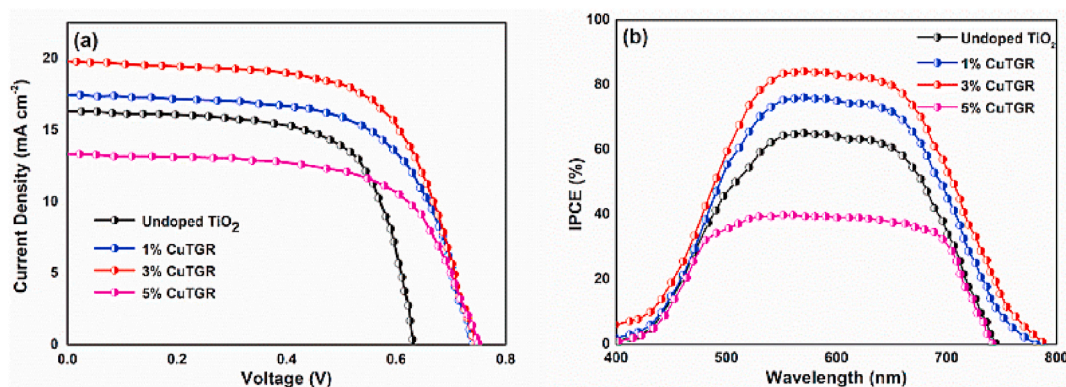
Fig. 11. (a) *J-V* characteristics and (b) IPCE of DSSCs with CuTGR and TiO$_2$ photoanode [127].

Table 7
Electrical parameters of N719-based DSSC with TiO$_2$ NW-NH$_2$/GO/Ag photoanode [128].

Photoanode material	V_{oc} (volts)	J_{sc} (mA cm^{-2})	FF (%)	PCE (%)
TiO$_2$ NWs	0.71	8.52	57	4.05
TiO2 NW-NH$_2$	0.71	9.24	58	4.50
TiO2 NW/GO	0.72	10.94	59	5.44
TiO2 NW-NH$_2$/GO	0.72	12.89	63	6.87
TiO2 NW-NH$_2$/Ag	0.74	13.05	65	7.37
TiO2 NW/GO/Ag	0.75	13.63	65	7.81
TiO2 NW-NH$_2$/GO/Ag	**0.76**	**15.09**	**65**	**8.76**

A hybrid of NiS$_2$ microspheres/graphene prepared by hydrothermal treatment was used aa s photoanode in N719 DSSCs [129]. The hybrid NiS/graphene photoanode devices produced a J_{sc}, V_{oc}, FF and PCE of 23.13 mA cm^{-2}, 0.89 V, 85% and 12.56%, respectively, which was more than a double improvement in comparison to NiS photoanode device with J_{sc}, V_{oc}, FF and PCE of 11.56 mA cm^{-2}, 0.63 V, 63% and 5.02%, respectively. The NiS and NiS/graphene photoanode devices exhibited R$_{ct}$ values of 8.9 and 3.9 Ω and charge lifetime values of 21.3 and 13.2 s, respectively. The remarkable improvement was attributed to the fast reduction of I_3^- ions, increased injection of charge and faster charge transport. The same group synthesized a hybrid of MoS/graphene by the hydrothermal route and utilized it as a photoanode in N719 DSSCs [130]. The hybrid and MoS-modified photoanode devices yielded a J_{sc}, V_{oc}, FF, PCE of 15.82 mA cm^{-2}, 0.82 V, 71%, 8.92% and 9.32 mA cm^{-2}, 0.67 V, 52%,3.36%, respectively. Again, they recorded a more than double performance enhancement attributed to increased optical absorption, light trapping, increased charge injection and decreased charge recombination. The R$_{ct}$ values were 10.5 and 7.5 Ω for MoS and MoS/graphene photoanode devices, respectively.

5.2.2. Counter electrode

Ag NPs doped graphene- Ba$_2$GaInO$_6$ (G-BGI@Ag) synthesized by hydrothermal method was used as CE in N719-based DSSCs [131]. Atomic percentages of the Ag solution were varied between 2 and 6%. The G-BGI@Ag CE at optimum concentration yielded better performance (*ca*. J_{sc}, V_{oc}, FF, PCE of 18.10 mA cm^{-2}, 0.79 V, 69%, 9.92%, respectively) than Pt CE (*ca*. J_{sc}, V_{oc}, FF, PCE of 17.10 mA cm^{-2}, 0.75 V, 62%, 7.99%, respectively). Ba$_2$GaInO$_6$ (BGI) CE device exhibited inferior performance (*ca*. J_{sc}, V_{oc}, FF, PCE of 12.90 mA cm^{-2}, 0.64 V, 63%, 5.20%, respectively), which improved upon the incorporation of GO (G-BGI) (*ca*. J_{sc}, V_{oc}, FF, PCE of 13.10 mA cm^{-2}, 0.68 V, 67%, 6.0%, respectively) because of the high surface area of GO, which increases the catalytic activity of the CE. The superior performance upon incorporating Ag was attributed to better charge transfer in the nanocomposite. G-BGI@Ag, G-BGI, BGI and Pt exhibited R$_{ct}$ of 0.35, 0.65, 0.61 and 0.49 Ω, respectively. Overall, the G-BGI@Ag CE showed superior catalytic activity.

CoNi$_2$S$_4$/rGO nanohybrid synthesized by a one-step hydrothermal route was used as CE in N719-based DSSCs [132]. The nanohybrid CE device realized a J_{sc}, V_{oc}, FF and PCE of 16.34 mA cm^{-2}, 0.67 V, 84% and 9.22%, respectively, which was comparable to the Pt CE device with J_{sc}, V_{oc}, FF and PCE of 16.45 mA cm^{-2}, 0.68 V, 85% and 9.51%, respectively. However, rGO Pt device performance was inferior *ca*. J_{sc}, V_{oc}, FF and PCE of 10.68 mA cm^{-2}, 0.55 V, 58% and 3.44%, respectively, while CoNi$_2$S$_4$ CE device yielded a J_{sc}, V_{oc}, FF and PCE of 13.14 mA cm^{-2}, 0.61 V, 72% and 5.78%, respectively. The nanohybrid CE performed better in terms of all the electrical parameters than either the CoNi$_2$S$_4$ or the rGO CE devices, showing the synergistic effect of the electrical conductivity of rGO and the catalytic activity of CoNi$_2$S$_4$ nanorods. The superior performance of the nanohybrid CE was attributed to dense small-sized nanorods uniformly distributed and well anchored on the rGO sheets. This formed charge percolation pathways and increased surface catalytic sites, which synergistically improved the electrocatalytic performance of the CE. Enhanced catalytic performance implies faster redox reduction reaction, which in turn causes faster dye regeneration, leading to the injection of more photoelectrons for high J_{sc} and FF values.

Mirzaei and Gholivand [11] synthesized amorphous RuS$_2$ NPs decorated on rGO by single-step hydrothermal route and used it as

CE in N719-DSSCs. The RuS$_2$/rGO CE device realized a J_{sc}, V_{oc}, FF and PCE of 20.64 mA cm^{-2}, 0.78 V, 52% and 8.37%, respectively, which was better than bare RuS$_2$ with J_{sc}, V_{oc}, FF and PCE of 20.41 mA cm^{-2}, 0.78 V, 46% and 7.32%, respectively. Incorporation of rGO improved the FF, implying better catalytic activity. The reference Pt CE yielded J_{sc}, V_{oc}, FF and PCE of 24.12 mA cm^{-2}, 0.76 V, 52% and 9.53%, respectively.

Nickel oxide@nickel sulphide@graphene (NiO@NiS@G) of hexagonal-shaped NiO@NiS anchored on graphene sheets was synthesized by hydrothermal method and used as the CE in N719 DSSCs [133]. NiO@NiS, NiO@NiS@G, and Pt CE devices yielded PCEs of 1.68, 2.10 and 2.77%, respectively. The R$_{ct}$ for the NiO@NiS, NiO@NiS@G and Pt CE was 38.6, 23.2 and 15.1 Ω, respectively. Graphene in the nanocomposite improved its electrical conductivity, thus leading to a decreased R$_{ct}$ compared to NiO@NiS. Similarly, graphene improved the electrochemical performance of the NiO@NiS@G composite CE.

Loading MNPs in the photoanode and CE of DSSCs comes with performance benefits. Firstly, it alters the energy levels, i. e the MNPs cause a negative potential shift in the Fermil level, thus improves V_{oc}. Secondly, it improves light absorption through the LSPR effect and increases dye loading. Again, the shape, size and morphology of the MNPs influence their LSPR effect. Nanowires and nanorods yield better results than spherically shaped MNPs because of increased surface area for dye loading. Core-shell structured MNPs perform better than bare ones as the shell helps with the engineering of the interfacial interaction between the plasmonic NSs and the TiO$_2$. Besides, it provides a protective layer on the photoanode against corrosion by electrolyte. Functionalization of the plasmonics with an amine group adds impetus to interfacial engineering. Further, hybrid NPs such as Au–Ag NPs provide better light harvesting because of complementary absorption at different wavelengths and the corporation of their plasmonic effects. Both the MNPs and GNMs in the photoanode increase the dye loading of TiO$_2$ for enhanced light absorption. Hybrids of MNPs/GNMs, given graphene's high surface area and 2D nature, increase the catalytic activity of CE. Furthermore, these hybrids improve charge transport of the photoanode, thus limits charge carrier recombination.

6. Conclusion

This review examined recent developments in the application of MNPs and hybrids of MNPs/GNMs in PSCs and DSSCs. Precisely, it has elucidated the potency of these nanomaterials in mitigating the poor optical absorption and charger carrier mobility of these devices for better photovoltaic performance. MNPs incorporated in PSCs promote photovoltaic performance through various mechanisms. In the photoactive medium, the MNPs promote light harvesting *via* enhanced light scattering, near-field effect, plasmon-induced charge separation and creation of optical solid absorption bands. MNPs embedded in the active layer promote light harvesting by creating strong electromagnetic fields within their vicinity, i. e, near-field effect. This effect is pronounced for small-sized MNPs and is compatible with solution-based device processing. MNPs promote light scattering in the active layer, increasing the optical path length and thus, resulting in improved light trapping and photon harvesting. Plasmon-induced charge separation by MNPs results from primary and secondary excitation of electron-hole pairs. For the interfacial layers of PSCs, MNPs can be incorporated in the ETL and HTL or placed at the HTL- ETL-active layer interface. This way, the MNPs improve light harvesting in the devices through far-field scattering and near-field effect. Also, the MNPs improve the charge extraction properties of the interfacial layers. Hybrids of MNPs/GNMs utilize the high carrier mobility and surface area of graphene, the LSPR effect of MNPs to improve the performance of PSCs. Using such hybrids in the interfacial layers improves charge extraction efficiency at the interface and light harvesting in the device by far-field scattering. Similarly, it leads to enhanced charge carrier mobility of the devices. Employing MNPs and/or hybrids of MNPs/GNMs simultaneously in the interfacial and active layers of PSCs leads to increased broadband optical absorption and better charge transport. Overall, the result of utilizing these nanomaterials in the PSCs is enhanced charge generation, separation, and transportation for better photovoltaic performance. Thus, this approach is fitting in circumventing the poor optical absorption and charge carrier mobilities in PSCs.

Incorporation of MNPs in the photoanode results in improved photovoltaic performance of DSSCs. The primary mechanism for this enhancement is increased optical absorption by the creation of new absorption bands and extended absorption wavelengths in the solar spectrum. Using MNPs as cosensitizers in DSSCs offer a complementary spectral response to the dye, thus yield improved optical absorption in the device. MNPs in the photoanode improve the V_{oc} of DSSCs through electron storage effects, which shifts the Fermi level to more negative potentials. MNPs promote charge separation *via* localized electromagnetic fields. Nonetheless, bare MNPs in the photoanode suffer from corrosion by the electrolyte, resulting in reduced device stability. Hence, having a thin protective layer (core-shell nanostructure) on the MNPs in the photoanode is imperative. Such a layer also aids in charge separation, thus reducing charge carrier recombination. Utilizing hybrids of MNPs/GNMs as CE or photoanode improves the photovoltaic performance of DSSCs. The high surface area of GNMs increases the surface area for dye adsorption and catalytic activity of the photoanode and CE, respectively. Synergy in the high electrical conductivity of GNMs and catalytic activity of both GNMs and MNPs leads to an enhanced electro-catalytic performance of the DSSCs. Such nanohybrids yield comparable photovoltaic performance to the standard Pt CE thus, are potential replacements for the relatively costly Pt.

7. Future perspective

Given the impacts of MNPS and hybrids of MNPs/GNMs on the performance of PSCs and DSSCs, it is imperative to consider utilizing these nanomaterials in solar cells. The light-harvesting properties of MNPs combined with the good electronic transport in graphene make these nanomaterials stand out in improving the performance of solar cells. The MNPs produce high optical absorption in a broad wavelength range in both PSCs and DSSCs. Besides, these nanomaterials can be easily loaded in the active and interfacial layers of PSCs and photoanode of DSSCs by simple solution phase methods. In DSSCs, plasmonic CEs yield comparable performance to Pt, thus, are a

suitable replacement, while plasmonic photoanodes yield better photovoltaic performance than the conventional TiO$_2$. In PSCs, these nanomaterials go a long way in enhancing optical absorption and charge transport. Further, these nanomaterials can be employed in other emerging solar conversion technologies to realize continued progress in solar energy conversion efficiencies. Nonetheless, in whichever solar energy conversion devices these nanomaterials are to be employed, the size and morphology of the MNPs, as well as their intercalation, should be tailored to maximise the LSPR effect.

Funding

CRediT authorship contribution statement

Tabitha A. Amollo: Writing – review & editing, Writing – original draft, Software, Resources, Project administration, Methodology, Investigation, Funding acquisition, Formal analysis, Data curation, Conceptualization.

Declaration of competing interest

The authors declare that they have no known competing financial interests or personal relationships that could have appeared to influence the work reported in this paper.

Appendix A. Supplementary data

Supplementary data related to this article can be found at https://doi.org/10.1016/j.heliyon.2024.e26401.

References

[1] T.A. Amollo, G.T. Mola, M. Kirui, V.O. Nyamori, Graphene for thermoelectric applications: prospects and challenges, Crit. Rev. Solid State Mater. Sci. 43 (2) (2018) 133–157, https://doi.org/10.1080/10408436.2017.1300871.

[2] X. Du, I. Skachko, A. Barker, E.Y. Andrei, Approaching ballistic transport in suspended graphene, Nat. Nanotechnol. 3 (8) (2008) 491–495, https://doi.org/10.1038/nnano.2008.199.

[3] A.K. Geim, K.S. Novoselov, The rise of graphene, Nat. Mater. 6 (2007) 183–191, https://doi.org/10.1038/nmat1849.

[4] T.A. Amollo, G.T. Mola, V.O. Nyamori, Reduced graphene oxide-germanium quantum dot nanocomposite: electronic, optical and magnetic properties, Nanotechnology 28 (49) (2017) 495703, https://doi.org/10.1088/1361-6528/aa9299.

[5] M. Auffan, J. Rose, M.R. Wiesner, J.-Y. Bottero, Chemical stability of metallic nanoparticles: a parameter controlling their potential cellular toxicity in vitro, Environ. Pollut. 157 (4) (2009) 1127–1133, https://doi.org/10.1016/j.envpol.2008.10.002.

[6] A.U. Khan, S. Zhao, G. Liu, Key parameter controlling the sensitivity of plasmonic metal nanoparticles: aspect ratio, J. Phys. Chem. C 120 (34) (2016) 19353–19364, https://doi.org/10.1021/acs.jpcc.6b06519.

[7] E.L. Lim, C.C. Yap, M.A.M. Teridi, C.H. Teh, M.H.H. Jumali, A review of recent plasmonic nanoparticles incorporated P3HT: PCBM organic thin film solar cells, Org. Electron. 36 (2016) 12–28, https://doi.org/10.1016/j.orgel.2016.05.029.

[8] F.-L. Meng, Z. Guo, X.-J. Huang, Graphene-based hybrids for chemiresistive gas sensors, TrAC- Trends Anal. Chem. 68 (2015) 37–47, https://doi.org/10.1016/j.trac.2015.02.008.

[9] A.V. Singhal, H. Charaya, I. Lahiri, Noble metal decorated graphene-based gas sensors and their fabrication: a review, Crit. Rev. Solid State Mater. Sci. 42 (6) (2017) 499–526, https://doi.org/10.1080/10408436.2016.1244656.

[10] K.T. Nguyen, Y. Zhao, Integrated graphene/nanoparticle hybrids for biological and electronic applications, Nanoscale 6 (12) (2014) 6245–6266, https://doi.org/10.1039/C4NR00612G.

[11] M. Mirzaei, M.B. Gholivand, Synthesis of ruthenium sulfide nanoparticles decorated on reduced graphene oxide/multi-walled carbon nanotubes as a catalytic counter electrode for dye-sensitized solar cells exceeding 13% efficiency, Sol. Energy 242 (2022) 212–224, https://doi.org/10.1016/j.solener.2022.07.010.

[12] K. Lü, G. Zhao, X. Wang, A brief review of graphene-based material synthesis and its application in environmental pollution management, Chinese Sci. Bull. 57 (11) (2012) 1223–1234, https://doi.org/10.1007/s11434-012-4986-5.

[13] W. Saeed, Z. Abbasi, S. Majeed, S.A. Shahzad, A.F. Khan, A.J. Shaikh, An insight into the binding behavior of graphene oxide and noble metal nanoparticles, J. Appl. Phys. 129 (12) (2021) 125302, https://doi.org/10.1063/5.0041894.

[14] M.E. Stewart, N.H. Mack, V. Malyarchuk, J.A. Soares, T.-W. Lee, S.K. Gray, R.G. Nuzzo, J.A. Rogers, Quantitative multispectral biosensing and 1D imaging using quasi-3D plasmonic crystals, P. Natl. A. Sci. 103 (46) (2006) 17143–17148, https://doi.org/10.1073/pnas.0606216103.

[15] H. Raether, Surface Plasmons on Smooth and Rough Surfaces and on Gratings, Springer Tracts in Modern Physics, Springer, Heidelberg, Berlin, 1988.

[16] K.A. Willets, R.P. Van Duyne, Localized surface plasmon resonance spectroscopy and sensing, Annu. Rev. Phys. Chem. 58 (1) (2007) 267–297, https://doi.org/10.1146/annurev.physchem.58.032806.104607.

[17] A.J. Haes, C.L. Haynes, A.D. McFarland, G.C. Schatz, R.P. Van Duyne, S. Zou, Plasmonic materials for surface-enhanced sensing and spectroscopy, MRS Bull. 30 (5) (2005) 368–375, https://doi.org/10.1557/mrs2005.100.

[18] S.A. Maier, Plasmonics: Fundamentals and Applications, vol. XXVI, Springer, Newyork, 2007.

[19] C.F. Bohren, D.R. Huffman, Absorption and Scattering of Light by Small Particles, John Wiley & Sons, 2008.

[20] U. Kreibig, M. Vollmer, Optical Properties of Metal Clusters, Springer, Germany, 2013.

[21] M.E. Stewart, C.R. Anderton, L.B. Thompson, J. Maria, S.K. Gray, J.A. Rogers, R.G. Nuzzo, Nanostructured plasmonic sensors, Chem. Rev. 108 (2) (2008) 494–521, https://doi.org/10.1021/cr068126n.

[22] K.L. Kelly, E. Coronado, L.L. Zhao, G.C. Schatz, The optical properties of metal nanoparticles: the influence of size, shape, and dielectric environment, J. Phys. Chem. B (2003) 668–677, https://doi.org/10.1021/jp026731y.

[23] N.L. Pacioni, C.D. Borsarelli, V. Rey, A.V. Veglia, in: E. I Alacorn, M. Griffith, K. I Udekwu (Eds.), Synthetic Routes for the Preparation of Silver Nanoparticles, Engineering Materials, Springer, Switzeland, 2015, pp. 13–46.

[24] Q. Zhang, Y.N. Tan, J. Xie, J.Y. Lee, Colloidal synthesis of plasmonic metallic nanoparticles, Plasmonics 4 (1) (2009) 9–22, https://doi.org/10.1007/s11468-008-9067-x.

[25] X. Zhao, C. Wei, Z. Gai, S. Yu, X. Ren, Chemical vapor deposition and its application in surface modification of nanoparticles, Chem. Pap. 74 (3) (2020) 767–778, https://doi.org/10.1007/s11696-019-00963-y.

[26] P.A. Pandey, G.R. Bell, J.P. Rourke, A.M. Sanchez, M.D. Elkin, B.J. Hickey, N.R. Wilson, Physical vapor deposition of metal nanoparticles on chemically modified graphene: observations on metal–graphene interactions, Small 7 (22) (2011) 3202–3210, https://doi.org/10.1002/smll.201101430.

[27] S.-C. Chen, D.-H. Hsieh, H. Jiang, Y.-K. Liao, F.-I. Lai, C.-H. Chen, C.W. Luo, J.-Y. Juang, Y.-L. Chueh, K.-H. Wu, Growth and characterization of Cu (In, Ga) Se₂ thin films by nanosecond and femtosecond pulsed laser deposition, Nanoscale Res. Lett. 9 (1) (2014) 1–7, https://doi.org/10.1186/1556-276X-9-280.

[28] J. Hasnidawani, H. Azlina, H. Norita, N. Bonnia, S. Ratim, E. Ali, Synthesis of ZnO nanostructures using sol-gel method, Procedia Chem. 19 (2016) 211–216, https://doi.org/10.1016/j.proche.2016.03.095.

[29] N.N.M. Zorkipli, N.H.M. Kaus, A.A. Mohamad, Synthesis of NiO nanoparticles through sol-gel method, Procedia Chem. 19 (2016) 626–631, https://doi.org/10.1016/j.proche.2016.03.062.

[30] Y. Yang, S. Matsubara, L. Xiong, T. Hayakawa, M. Nogami, Solvothermal synthesis of multiple shapes of silver nanoparticles and their SERS properties, J. Phys. Chem. C 111 (26) (2007) 9095–9104, https://doi.org/10.1021/jp068859b.

[31] S. Landage, A. Wasif, P. Dhuppe, Synthesis of nanosilver using chemical reduction methods, Int. J. Adv. Res. Eng. App. Sci. 3 (5) (2014) 14–22.

[32] Q.-l. Zhang, Z.-M. Yang, B.-j. Ding, X.-z. Lan, Y.-j. Guo, Preparation of copper nanoparticles by chemical reduction method using potassium borohydride, T. Nonferr. Metal Soc. 20 (2010) 240–244, https://doi.org/10.1016/S1003-6326(10)60047-7.

[33] E. Maryanti, D. Damayanti, I. Gustian, Synthesis of ZnO nanoparticles by hydrothermal method in aqueous rinds extracts of Sapindus rarak DC, Mater. Lett. 118 (2014) 96–98, https://doi.org/10.1016/j.matlet.2013.12.044.

[34] E. Borsella, R. D'Amato, G. Terranova, M. Falconieri, F. Fabbri, Synthesis of nanoparticles by laser pyrolysis: from research to applications, ENEA Mag 4 (2011) 54–64.

[35] M.T. Swihart, Vapor-phase synthesis of nanoparticles, Curr. Opin. Colloid Interface Sci. 8 (1) (2003) 127–133, https://doi.org/10.1016/S1359-0294(03)00007-4.

[36] P. Majerič, B. Friedrich, R. Rudolf, Au-nanoparticle synthesis via ultrasonic spray pyrolysis with a separate evaporation zone, Materiali in Tehnologije 5 (49) (2015) 791–796, https://doi.org/10.17222/mit.2014.264.

[37] H.R. Ghaffarian, M. Saiedi, M.A. Sayyadnejad, A.M. Rashidi, Synthesis of ZnO nanoparticles by spray pyrolysis method, Iran, J. Chem. Chem. Eng. 30 (2011) 1–6.

[38] T.P. Yadav, R.M. Yadav, D.P. Singh, Mechanical milling: a top down approach for the synthesis of nanomaterials and nanocomposites, Nanosci. Nanotech. 2 (3) (2012) 22–48, https://doi.org/10.5923/j.nn.20120203.01.

[39] M. Ullah, M. Ali, S.B. Abd Hamid, Surfactant-assisted ball milling: a novel route to novel materials with controlled nanostructure-A review, Rev. Adv. Mater. Sci. 37 (2014) 1–14.

[40] M. Seyedi, S. Haratian, J.V. Khaki, Mechanochemical synthesis of Fe2O3 nanoparticles, Procedia Materials Science 11 (2015) 309–313, https://doi.org/10.1016/j.mspro.2015.11.093.

[41] K. Ralphs, C. D'Agostino, R. Burch, S. Chansai, L.F. Gladden, C. Hardacre, S.L. James, J. Mitchell, S.F. Taylor, Assessing the surface modifications following the mechanochemical preparation of a Ag/Al₂O₃ selective catalytic reduction catalyst, Catal. Sci. Technol. 4 (2) (2014) 531–539, https://doi.org/10.1039/C3CY00945A.

[42] G.E. Johnson, T. Moser, M. Engelhard, N.D. Browning, J. Laskin, Fabrication of electrocatalytic Ta nanoparticles by reactive sputtering and ion soft landing, J. Chem. Phys. 145 (17) (2016) 174701, https://doi.org/10.1063/1.4966199.

[43] M. Nie, K. Sun, D.D. Meng, Formation of metal nanoparticles by short-distance sputter deposition in a reactive ion etching chamber, J. Appl. Phys. 106 (5) (2009) 054314, https://doi.org/10.1063/1.3211326.

[44] A. Simakin, V. Voronov, N. Kirichenko, G. Shafeev, Nanoparticles produced by laser ablation of solids in liquid environment, Appl. Phys A 79 (4) (2004) 1127–1132, https://doi.org/10.1007/s00339-004-2660-8.

[45] H.R. Ghorbani, A review of methods for synthesis of Al nanoparticles, Orient, J. Chem. 30 (4) (2014) 1941–1949, https://doi.org/10.13005/ojc/300456.

[46] N. Semaltianos, Nanoparticles by laser ablation, Crit. Rev. Solid State Mater. Sci. 35 (2) (2010) 105–124, https://doi.org/10.1080/10408431003788233.

[47] M. Scuderi, M. Esposito, F. Todisco, D. Simeone, I. Tarantini, L. De Marco, M. De Giorgi, G. Nicotra, L. Carbone, D. Sanvitto, Nanoscale study of the tarnishing process in electron beam lithography-fabricated silver nanoparticles for plasmonic applications, J. Phys. Chem. C 120 (42) (2016) 24314–24323, https://doi.org/10.1021/acs.jpcc.6b03963.

[48] O. Romanenko, P. Slepička, P. Malinsky, M. Cutroneo, V. Havránek, J. Stammers, V. Švorčík, A. Macková, The influence of Au-nanoparticles presence in PDMS on microstructures creation by ion beam lithography, Surf. Interface Anal. 52 (12) (2020) 1040–1044, https://doi.org/10.1002/sia.6821.

[49] S. Low, Y.-S. Shon, Molecular interactions between pre-formed metal nanoparticles and graphene families, Adv. Nano Res. 6 (4) (2018) 357.

[50] R. Bhaskar, H. Joshi, A.K. Sharma, A.K. Singh, Reusable catalyst for transfer hydrogenation of aldehydes and ketones designed by anchoring palladium as nanoparticles on graphene oxide functionalized with selenated amine, ACS Appl. Mater. Inter. 9 (3) (2017) 2223–2231.

[51] A.E. Vilian, S.R. Choe, K. Giribabu, S.-C. Jang, C. Roh, Y.S. Huh, Y.-K. Han, Pd nanospheres decorated reduced graphene oxide with multi-functions: highly efficient catalytic reduction and ultrasensitive sensing of hazardous 4-nitrophenol pollutant, J. Hazard Mater. 333 (2017) 54–62, https://doi.org/10.1021/acsami.6b10457.

[52] N. Wang, B. Guan, Y. Zhao, Y. Zou, G. Geng, P. Chen, F. Wang, M. Liu, Sub-10 nm Ag Nanoparticles/graphene oxide: Controllable synthesis, size-dependent and extremely ultrahigh catalytic activity, Small 15 (23) (2019) 1901701, https://doi.org/10.1002/smll.201901701.

[53] K.-C. Hsu, D.-H. Chen, Microwave-assisted green synthesis of Ag/reduced graphene oxide nanocomposite as a surface-enhanced Raman scattering substrate with high uniformity, Nanoscale Res. Lett. 9 (1) (2014) 1–9, https://doi.org/10.1186/1556-276X-9-193.

[54] X. Huang, G. Zhao, X. Wang, Fabrication of reduced graphene oxide/metal (Cu, Ni, Co) nanoparticle hybrid composites via a facile thermal reduction method, RSC Adv. 5 (62) (2015) 49973–49978, https://doi.org/10.1039/C5RA08670A.

[55] K. Ueno, T. Oshikiri, Q. Sun, X. Shi, H. Misawa, Solid-state plasmonic solar cells, Chem. Rev. 118 (6) (2017) 2955–2993.

[56] K.a. Catchpole, A. Polman, Plasmonic solar cells, Opt Express 16 (26) (2008) 21793–21800, https://doi.org/10.1021/acs.chemrev.7b00235.

[57] K. Catchpole, A. Polman, Design principles for particle plasmon enhanced solar cells, Appl. Phys. Lett. 93 (19) (2008) 191113, https://doi.org/10.1063/1.3021072.

[58] H.A. Atwater, A. Polman, Plasmonics for improved photovoltaic devices, Nat. Mater. 9 (3) (2010) 205–213, https://doi.org/10.1038/nmat2629.

[59] S.-W. Baek, J. Noh, C.-H. Lee, B. Kim, M.-K. Seo, J.-Y. Lee, Plasmonic forward scattering effect in organic solar cells: a powerful optical engineering method, Sci. Rep. 3 (1) (2013) 1–7, https://doi.org/10.1038/srep01726.

[60] F. Beck, A. Polman, K. Catchpole, Tunable light trapping for solar cells using localized surface plasmons, J. Appl. Phys. 105 (11) (2009) 114310, https://doi.org/10.1063/1.3140609.

[61] S. Mokkapati, F. Beck, A. Polman, K. Catchpole, Designing periodic arrays of metal nanoparticles for light-trapping applications in solar cells, Appl. Phys. Lett. 95 (5) (2009) 053115, https://doi.org/10.1063/1.3200940.

[62] C. Fei Guo, T. Sun, F. Cao, Q. Liu, Z. Ren, Metallic nanostructures for light trapping in energy-harvesting devices, Light Sci. Appl. 3 (4) (2014), https://doi.org/10.1038/lsa.2014.42 e161-e161.

[63] C.C. Wang, W.C. Choy, C. Duan, D.D. Fung, E. Wei, F.-X. Xie, F. Huang, Y. Cao, Optical and electrical effects of gold nanoparticles in the active layer of polymer solar cells, J. Mater. Chem. 22 (3) (2012) 1206–1211, https://doi.org/10.1039/C1JM14150C.

[64] M.A. Green, S. Pillai, Harnessing plasmonics for solar cells, Nat. Photonics 6 (3) (2012) 130–132, https://doi.org/10.1038/nphoton.2012.30.

[65] R. Sundararaman, P. Narang, A.S. Jermyn, W.A. Goddard III, H.A. Atwater, Theoretical predictions for hot-carrier generation from surface plasmon decay, Nat. Commun. 5 (1) (2014) 1–8, https://doi.org/10.1038/ncomms6788.

[66] M.L. Brongersma, N.J. Halas, P. Nordlander, Plasmon-induced hot carrier science and technology, Nat. Nanotechnol. 10 (1) (2015) 25–34.

[67] E. Knoesel, A. Hotzel, T. Hertel, M. Wolf, G. Ertl, Dynamics of photoexcited electrons in metals studied with time-resolved two-photon photoemission, Surf. Sci. 368 (1–3) (1996) 76–81, https://doi.org/10.1038/nnano.2014.311.

[68] Y.K. Lee, H. Lee, C. Lee, E. Hwang, J.Y. Park, Hot-electron-based Sol. Energy conversion with metal–semiconductor nanodiodes, J. Phys.: Condens. Mat. 28 (25) (2016) 254006, https://doi.org/10.1088/0953-8984/28/25/254006.

[69] E. Knoesel, A. Hotzel, M. Wolf, Ultrafast dynamics of hot electrons and holes in copper: excitation, energy relaxation, and transport effects, Phys. Rev. B 57 (20) (1998) 12812, https://doi.org/10.1103/PhysRevB.57.12812.

[70] C. Clavero, Plasmon-induced hot-electron generation at nanoparticle/metal-oxide interfaces for photovoltaic and photocatalytic devices, Nat. Photonics 8 (2) (2014) 95–103, https://doi.org/10.1038/nphoton.2013.238.

[71] W.R. Erwin, H.F. Zarick, E.M. Talbert, R. Bardhan, Light trapping in mesoporous solar cells with plasmonic nanostructures, Energ. Environmen. Sci. 9 (5) (2016) 1577–1601, https://doi.org/10.1039/C5EE03847B.

[72] M.S. Hamed, M.A. Adedeji, Y. Zhang, G.T. Mola, Silver sulphide nano-particles enhanced photo-current in polymer solar cells, Appl. Phys. A 126 (3) (2020) 1–9, https://doi.org/10.1007/s00339-020-3389-8.

[73] M.W. Dlamini, M.S. Hamed, X.G. Mbuyise, G.T. Mola, Improved energy harvesting using well-aligned ZnS nanoparticles in bulk-heterojunction organic solar cell, J. Mater. Sci. Mater. Electron. 31 (12) (2020) 9415–9422, https://doi.org/10.1007/s10854-020-03481-w.

[74] A. Das, K. Kumar, A. Dhawan, Plasmonics-enhanced Organic Solar Cells with Complex Metallic Nanoparticles, Photonics for Solar Energy Systems VIII, SPIE, 2020, pp. 15–20, https://doi.org/10.1117/12.2555583.

[75] X.-H. Liu, L.-X. Hou, J.-F. Wang, B. Liu, Z.-S. Yu, L.-Q. Ma, S.-P. Yang, G.-S. Fu, Plasmonic-enhanced polymer solar cells with high efficiency by addition of silver nanoparticles of different sizes in different layers, Sol. Energy 110 (2014) 627–635, https://doi.org/10.1016/j.solener.2014.06.019.

[76] Y. Thaver, S.O. Oseni, G.T. Mola, Silver doped nickel oxide nanocomposite and photon harvesting enhancement in bulkheterojunction organic solar cell, Sol. Energy 214 (2021) 11–18, https://doi.org/10.1016/j.solener.2020.11.044.

[77] S.L. Mousavi, F. Jamali-Sheini, M. Sabaeian, R. Yousefi, Enhanced solar cell performance of P3HT: PCBM by SnS nanoparticles, Sol. Energy 199 (2020) 872–884, https://doi.org/10.1016/j.solener.2020.02.031.

[78] M. Omrani, H. Fallah, K.-L. Choy, M. Abdi-Jalebi, Impact of hybrid plasmonic nanoparticles on the charge carrier mobility of P3HT: PCBM polymer solar cells, Sci. Rep. 11 (1) (2021) 1–12, https://doi.org/10.1038/s41598-021-99095-1.

[79] X. Xu, A.K.K. Kyaw, B. Peng, Q. Xiong, H.V. Demir, Y. Wang, T.K. Wong, X.W. Sun, Influence of gold-silica nanoparticles on the performance of small-molecule bulk heterojunction solar cells, Org. Electron. 22 (2015) 20–28, https://doi.org/10.1016/j.orgel.2015.03.026.

[80] W.-H. Tseng, C.-Y. Chiu, S.-W. Chou, H.-C. Chen, M.-L. Tsai, Y.-C. Kuo, D.-H. Lien, Y.-C. Tsao, K.-Y. Huang, C.-T. Yeh, Shape-dependent light harvesting of 3D gold nanocrystals on bulk heterojunction solar cells: plasmonic or optical scattering effect? J. Phys. Chem. C 119 (14) (2015) 7554–7564.

[81] P. Tonui, G.T. Mola, Improved charge extraction in polymer solar cell using metal nano-composite, Physica E 107 (2019) 154–159, https://doi.org/10.1021/jp512192e.

[82] L.-W. Jang, H. Park, S.-H. Lee, A.Y. Polyakov, R. Khan, J.-K. Yang, I.-H. Lee, Device performance of inverted polymer solar cells with AgSiO₂ nanoparticles in active layer, Opt Express 23 (7) (2015) A211–A218, https://doi.org/10.1364/OE.23.00A211.

[83] S.H. Oh, S.J. Heo, J.S. Yang, H.J. Kim, Effects of ZnO nanoparticles on P3HT: PCBM organic solar cells with DMF-modulated PEDOT: PSS buffer layers, ACS Appl. Mater. Inter. 5 (22) (2013) 11530–11534, https://doi.org/10.1021/am4046475.

[84] J. Ajuria, I. Etxebarria, E. Azaceta, R. Tena-Zaera, N. Fernandez-Montcada, E. Palomares, R. Pacios, Novel ZnO nanostructured electrodes for higher power conversion efficiencies in polymeric solar cells, Phys. Chem. Chem. Phys. 13 (46) (2011) 20871–20876, https://doi.org/10.1039/C1CP22830G.

[85] M. Iqbal, M.A.Z.G. Sial, S. Shabbir, M. Siddiq, A. Iqbal, Effect of Fe doping on the crystallinity of CuO nanotubes and the efficiency of the hybrid solar cells, J. Photochem. Photobio. A: Chemistry 335 (2017) 112–118, https://doi.org/10.1016/j.jphotochem.2016.11.020.

[86] A.P. Wanninayake, S. Gunasekar, S. Li, B.C. Church, N. Abu-Zahra, Performance enhancement of polymer solar cells using copper oxide nanoparticles, Semicond. Sci. Tech. 30 (6) (2015) 064004, https://doi.org/10.1088/0268-1242/30/6/064004.

[87] A.P. Wanninayake, B.C. Church, N. Abu-Zahra, CuO NPs incorporated single and double junction polymer solar cells, Exp. Theo. Nanotechnology (2018) 31–42, https://doi.org/10.56053/2.1.31.

[88] T.A. Amollo, G.T. Mola, V.O. Nyamori, Organic solar cells: materials and prospects of graphene for active and interfacial layers, Crit. Rev. Solid State Mater. Sci. 45 (4) (2020) 261–288, https://doi.org/10.1080/10408436.2019.1632791.

[89] S.B. Dkhil, D. Duché, M. Gaceur, A.K. Thakur, F.B. Aboura, L. Escoubas, J.J. Simon, A. Guerrero, J. Bisquert, G. Garcia-Belmonte, Interplay of optical, morphological, and electronic effects of ZnO optical spacers in highly efficient polymer solar cells, Adv. Energy Mater. 4 (18) (2014) 1400805, https://doi.org/10.1002/aenm.201400805.

[90] M. Notarianni, K. Vernon, A. Chou, M. Aljada, J. Liu, N. Motta, Plasmonic effect of gold nanoparticles in organic solar cells, Sol. Energy 106 (2014) 23–37, https://doi.org/10.1016/j.solener.2013.09.026.

[91] A. Singh, A. Dey, P.K. Iyer, Collective effect of hybrid Au-Ag nanoparticles and organic-inorganic cathode interfacial layers for high performance polymer solar cell, Sol. Energy 173 (2018) 429–436, https://doi.org/10.1016/j.solener.2018.07.052.

[92] A.S. Sarkar, A.D. Rao, A. Jagdish, A. Gupta, C.K. Nandi, P.C. Ramamurthy, S.K. Pal, Facile embedding of gold nanostructures in the hole transporting layer for efficient polymer solar cells, Org. Electron. 54 (2018) 148–153, https://doi.org/10.1016/j.orgel.2017.12.029.

[93] S.R. Gollu, R. Sharma, G. Srinivas, S. Kundu, D. Gupta, Incorporation of silver and gold nanostructures for performance improvement in P3HT: PCBM inverted solar cell with rGO/ZnO nanocomposite as an electron transport layer, Org. Electron. 29 (2016) 79–87, https://doi.org/10.1016/j.orgel.2015.11.015.

[94] R. Sharma, F. Alam, A. Sharma, V. Dutta, S. Dhawan, ZnO anchored graphene hydrophobic nanocomposite-based bulk heterojunction solar cells showing enhanced short-circuit current, J. Mater. Chem. C 2 (38) (2014) 8142–8151, https://doi.org/10.1039/C4TC01056F.

[95] S. Wanwong, W. Sangkhun, J. Wootthikanokkhan, The effect of co-sensitization methods between N719 and boron dipyrromethene triads on dye-sensitized solar cell performance, RSC Adv. 8 (17) (2018) 9202–9210.

[96] L. Yu, K. Fan, T. Duan, X. Chen, R. Li, T. Peng, Efficient panchromatic light harvesting with co-sensitization of zinc phthalocyanine and bithiophene-based organic dye for dye-sensitized solar cells, ACS Sustain. Chem. Eng. 2 (4) (2014) 718–725, https://doi.org/10.1039/C8RA00862K.

[97] V. Bhullar, D. Devi, F. Singh, S. Chopra, A. Debnath, D. Aswal, A. Mahajan, Ag implanted TiO₂ nanoparticle/nanofibers composites for dye sensitized solar cells applications, Sol. Energy 241 (2022) 109–119, https://doi.org/10.1016/j.solener.2022.06.009.

[98] R. Selvapriya, T. Abhijith, V. Ragavendran, V. Sasirekha, V. Reddy, J. Pearce, J. Mayandi, Impact of coupled plasmonic effect with multishaped silver nanoparticles on efficiency of dye sensitized solar cells, J. Alloy Compd. 894 (2022) 162339, https://doi.org/10.1016/j.jallcom.2021.162339.

[99] N. Shamsudin, S. Shafie, M.A. Ab Kadir, F. Ahmad, Y. Sulaiman, S. Chachuli, M. Razali, Flexible back-illuminated dye sensitised solar cells (DSSCs) with titanium dioxide/silver nanoparticles composite photoanode for improvement of power conversion efficiency, Optik 272 (2023) 170237, https://doi.org/10.1016/j.ijleo.2022.170237.

[100] K.B. Bhojanaa, J.J. Mohammed, M. Manishvarun, A. Pandikumar, Dye-sensitized solar cells with efficiency enhancement surpassing 65% through layer-by-layer assembled plasmonic photoanodes, J. Power Sources 558 (2023) 232593, https://doi.org/10.1016/j.jpowsour.2022.232593.

[101] H. Ran, J. Fan, X. Zhang, J. Mao, G. Shao, Enhanced performances of dye-sensitized solar cells based on Au-TiO₂ and Ag-TiO₂ plasmonic hybrid nanocomposites, Appl. Surf. Sci. 430 (2018) 415–423, https://doi.org/10.1016/j.apsusc.2017.07.107.

[102] K. Salimi, A. Atilgan, M.Y. Aydin, H. Yildirim, N. Celebi, A. Yildiz, Plasmonic mesoporous core-shell Ag-Au@ TiO₂ photoanodes for efficient light harvesting in dye sensitized solar cells, Sol. Energy 193 (2019) 820–827, https://doi.org/10.1016/j.solener.2019.10.039.

[103] S.W. Sheehan, H. Noh, G.W. Brudvig, H. Cao, C.A. Schmuttenmaer, Plasmonic enhancement of dye-sensitized solar cells using core–shell–shell nanostructures, J. Phys. Chem. C 117 (2) (2013) 927–934, https://doi.org/10.1021/jp311881k.

[104] Q. Liu, Y. Sun, M. Yao, B. Xu, G. Liu, M.B. Hussain, K. Jiang, C. Li, Au@ Ag@ Ag₂S heterogeneous plasmonic nanorods for enhanced dye-sensitized solar cell performance, Sol. Energy 185 (2019) 290–297, https://doi.org/10.1016/j.solener.2019.04.079.

[105] H. Choi, Y.-S. Chen, K.G. Stamplecoskie, P.V. Kamat, Boosting the photovoltage of dye-sensitized solar cells with thiolated gold nanoclusters, J. Phys. Chem. Lett. 6 (1) (2015) 217–223, https://doi.org/10.1021/jz502485w.

[106] G. Arthi, R. Selvam, C. Muthamizhchelvan, Y. Hayakawa, S.G. Ramaraj, Thorn-like morphology of TiO2 hierarchical structures and dye-sensitized solar cell characteristics, Mat. Lett. (2023) 134654, https://doi.org/10.1016/j.matlet.2023.134654.

[107] J. Manju, S. Amjith, L.P. Suresh, Synthesis of TiO2 nanoparticles and the performance of dye-sensitized solar cells, Mater. Today-Proc. (2023), https://doi.org/10.1016/j.matpr.2023.02.265.

[108] M. Roudgar-Amoli, Z. Shariatinia, Synergistic influence of plasmonic Ag nanoparticles/La0.6Sr0.4CoO3/TiO2 heterostructured photoanodes boosted solar energy harvesting by dye-sensitized photovoltaics, Sol. Energy 252 (2023) 101–126, https://doi.org/10.1016/j.solener.2023.01.049.

[109] H. Choi, W.T. Chen, P.V. Kamat, Know thy nano neighbor. Plasmonic versus electron charging effects of metal nanoparticles in dye-sensitized solar cells, ACS Nano 6 (5) (2012) 4418–4427, https://doi.org/10.1021/nn301137r.

[110] N. Chander, M.R. Samantaray, A comparative study of plasmonic dye-sensitized solar cells utilizing dielectric shell coated and uncoated Au nanoparticles, IEEE J. Photovolt. 11 (5) (2021) 1213–1221, https://doi.org/10.1109/JPHOTOV.2021.3086440.

[111] W.-L. Liu, F.-C. Lin, Y.-C. Yang, C.-H. Huang, S. Gwo, M.H. Huang, J.-S. Huang, The influence of shell thickness of Au@TiO2 core–shell nanoparticles on the plasmonic enhancement effect in dye-sensitized solar cells, Nanoscale 5 (17) (2013) 7953–7962, https://doi.org/10.1039/C3NR02800C.

[112] M. Yu, J. Zhang, S. Li, Y. Meng, J. Liu, Multi-functional DNA-based synthesis of SWNTs@(TiO2/Ag/Au) nanocomposites for enhanced light-harvesting and charge collection in DSSCs, RSC Adv. 5 (8) (2015) 5604–5610, https://doi.org/10.1039/C4RA12299B.

[113] M. Fallah, I. Maleki, M.-R. Zamani-Meymian, Y. Abdi, Enhancing the efficiency of dye-sensitized solar cell by increasing the light trapping and decreasing the electron-hole recombination rate due to Ag@ TiO2 core-shell photoanode structure, Mater. Res. Express 7 (1) (2019) 016409, https://doi.org/10.1088/2053-1591/ab5c8a.

[114] P. Nbelayim, G. Kawamura, W. Kian Tan, H. Muto, A. Matsuda, Systematic characterization of the effect of Ag@TiO2 nanoparticles on the performance of plasmonic dye-sensitized solar cells, Sci. Rep. 7 (1) (2017) 1–12, https://doi.org/10.1038/s41598-017-15541-z.

[115] Y.X. Dong, X.L. Wang, E.M. Jin, S.M. Jeong, B. Jin, S.H. Lee, One-step hydrothermal synthesis of Ag decorated TiO2 nanoparticles for dye-sensitized solar cell application, Renew. Energ. 135 (2019) 1207–1212, https://doi.org/10.1016/j.renene.2018.12.062.

[116] S. Rajkumar, M. Venkatraman, P. Balraju, K. Suguna, A. Pugazhendhi, Performance of simple green synthesized Ag incorporated TiO2 nanoparticles based photoanodes by doctor-blade coating as working electrodes for dye sensitized solar cells, Prog. Org. Coat. 164 (2022) 106697, https://doi.org/10.1016/j.porgcoat.2021.106697.

[117] D. Kabir, T. Forhad, W. Ghann, B. Richards, M.M. Rahman, M.N. Uddin, M.R.J. Rakib, M.H. Shariare, F.I. Chowdhury, M.M. Rabbani, Dye-sensitized solar cell with plasmonic gold nanoparticles modified photoanode, Nano-Structures & Nano-Objects 26 (2021) 100698, https://doi.org/10.1016/j.nanoso.2021.100698.

[118] I. Madigasekara, H. Perera, J. Kumari, G. Senadeera, M. Dissanayake, Photoanode modification of dye-sensitized solar cells with Ag/AgBr/TiO2 nanocomposite for enhanced cell efficiency, Sol. Energy 230 (2021) 59–72, https://doi.org/10.1016/j.solener.2021.10.015.

[119] V. Manikandan, A. Palai, A. Ramadoss, S. Mohanty, M. Navaneethan, Plasmon enfolded TiO2 hierarchical photoanode: fabrication and the performance evaluation as liquid-based dye-sensitized solar cell, J. Mater. Sci. Mater. Electron. 33 (11) (2022) 8655–8664, https://doi.org/10.1007/s10854-021-06724-6.

[120] G.A. Alamu, O. Adedokun, I.T. Bello, Y.K. Sanusi, Plasmonic enhancement of visible light absorption in Ag-TiO2 based dye-sensitized solar cells, Chemical Physics Impact 3 (2021) 100037, https://doi.org/10.1016/j.chphi.2021.100037.

[121] Y. Wang, J. Zhai, Y. Song, Plasmonic cooperation effect of metal nanomaterials at Au–TiO2–Ag interface to enhance photovoltaic performance for dye-sensitized solar cells, RSC Adv. 5 (1) (2015) 210–214, https://doi.org/10.1039/C4RA08753D.

[122] M.A. Al-Azawi, N. Bidin, M. Bououdina, S.M. Mohammad, Preparation of gold and gold–silver alloy nanoparticles for enhancement of plasmonic dye-sensitized solar cells performance, Sol. Energy 126 (2016) 93–104, https://doi.org/10.1016/j.solener.2015.12.043.

[123] K. Bhojanaa, M. Ramesh, A. Pandikumar, Complementary properties of silver nanoparticles on the photovoltaic performance of titania nanospheres based photoanode in dye-sensitized solar cells, Mater. Res. Bull. 122 (2020) 110672.

[124] Y. Xu, H. Zhang, X. Li, W. Wang, J. Li, Ag-encapsulated single-crystalline anatase TiO2 nanoparticle photoanodes for enhanced dye-sensitized solar cell performance, J. Alloy Compd. 695 (2017) 1104–1111, https://doi.org/10.1016/j.materresbull.2020.110672.

[125] H.-J. Hwang, S.-J. Joo, S.A. Patil, H.-S. Kim, Efficiency enhancement in dye-sensitized solar cells using the shape/size-dependent plasmonic nanocomposite photoanodes incorporating silver nanoplates, Nanoscale 9 (23) (2017) 7960–7969.

[126] P. Mahajan, R. Datt, V. Gupta, S. Arya, Synthesis and characterization of ZnO@ WO3 core/shell nanoparticles as counter electrode for dye-sensitized solar cell, Surface. Interfac. 30 (2022) 101920, https://doi.org/10.1039/C7NR01059A.

[127] M. Dhonde, K. Sahu, V. Murty, Cu-doped TiO2 nanoparticles/graphene composites for efficient dye-sensitized solar cells, Sol. Energy 220 (2021) 418–424, https://doi.org/10.1016/j.solener.2021.03.072.

[128] M. Kandasamy, M. Selvaraj, C. Kumarappan, S. Murugesan, Plasmonic Ag nanoparticles anchored ethylenediamine modified TiO2 nanowires@ graphene oxide composites for dye-sensitized solar cell, J. Alloy Compd. 902 (2022) 163743, https://doi.org/10.1016/j.jallcom.2022.163743.

[129] D. Krishnamoorthy, A. Prakasam, Low-cost and novel preparation of porous NiS2/graphene heterojunctions photoanodes for high-efficiency dye-sensitized solar cells, Inorg. Chem. Commun. 119 (2020) 108063, https://doi.org/10.1016/j.inoche.2020.108063.

[130] D. Krishnamoorthy, A. Prakasam, Preparation of MoS2/graphene nanocomposite-based photoanode for dye-sensitized solar cells (DSSCs), Inorg. Chem. Commun. 118 (2020) 108016, https://doi.org/10.1016/j.inoche.2020.108016.

[131] W.-C. Oh, S. Chanthai, Y. Areerob, Novel flexible Ag nanoparticles doped on graphene–Ba2GaInO6 as cathode material for enhancement in the power conversion of DSSCs, Sol. Energy 180 (2019) 510–518, https://doi.org/10.1016/j.solener.2019.01.033.

[132] A. Sarkar, S. Bera, A.K. Chakraborty, CoNi2S4-reduced graphene oxide nanohybrid: an excellent counter electrode for Pt-free DSSC, Sol. Energy 208 (2020) 139–149, https://doi.org/10.1016/j.solener.2020.07.075.

[133] K. Silambarasan, J. Archana, S. Athithya, S. Harish, R.S. Ganesh, M. Navaneethan, S. Ponnusamy, C. Muthamizhchelvan, K. Hara, Y. Hayakawa, Hierarchical NiO@NiS@ graphene nanocomposite as a sustainable counter electrode for Pt free dye-sensitized solar cell, Appl. Surf. Sci. 501 (2020) 144010, https://doi.org/10.1016/j.apsusc.2019.144010.